Eidgenössische Technische Hochschule Zürich
Swiss Federal Institute of Technology Zurich

Simulations and measurements of high-frequency transmons for a quantum transduction experiment

Master's Thesis

Luca Ben Herrmann

heluca@ethz.ch

Laboratory for Solid State Physics
Department of Physics, D-PHYS
ETH Zürich

Supervisors:
Prof. Yiwen Chu
Tom Schatteburg
Dr. Rodrigo Benevides

April 2, 2024

Acknowledgements

First and foremost, I would like to thank Tom Schatteburg for supervising my project with great guidance and support. Thank you for answering all my questions with attention to detail, for teaching me new things in the lab and for always being available to discuss my measurements and simulations. I could not have asked for better supervision for this project. I would also like to thank Rodrigo Benevides for co-supervising this project. Thank you for fabricating the qubits that I measured throughout this work and for being available for insightful discussions.

I would like to extend my gratitude to Professor Yiwen Chu for allowing me to perform this master's thesis in her group, for being available to discuss my work and for cultivating a friendly and welcoming environment in the group.

I would like to thank all members of the HYQU group. Specifically: Max Drimmer for fabricating the HBAR which I measured in this work, Stefano Marti for helping me debug code that I used for my measurements and Yu Yang for helping me with measuring the devices.

Lastly, I would like to thank my family, and especially my parents, for supporting me in every way possible throughout my studies.

Abstract

In recent years, substantial progress has been made in the field of circuit quantum acoustodynamics (cQAD) that suggests that a high-overtone bulk acoustic resonator (HBAR) can be used as an intermediary between the microwave and optical regime, thereby opening the possibility to transduce a quantum state from a superconducting qubit to an infrared photon [1–4]. A possible architecture of a quantum transducer consists of flip-chip bonding a qubit chip to an HBAR and placing the two chips inside an optical cavity that supports light in the optical regime. In this work, we focus on simulations and measurements of the high-frequency qubit needed to build such a quantum transducer as well as study its electromechanical coupling to an HBAR.

We measured three high-frequency transmon qubits at frequencies of around 13 GHz. The longest T_1 and T_2 times measured were $T_1 = 6.5 \pm 0.7$ μs and $T_2 = 1.8 \pm 0.2$ μs. Additionally, a hybrid device, consisting of a high-frequency transmon flip-chip bonded to an HBAR was characterized, and an electromechanical coupling strength of 1.38 ± 0.02 MHz was measured. An improved redesign of the on-chip readout resonator used to readout the state of the qubit has been proposed and simulations of the redesign are discussed. Through simulations, we could conclude that the measured coupling strength is an effective coupling strength to one collective mode consisting of many higher-order transverse mechanical modes.

Contents

Chapter 1

Introduction

In recent years, significant advancements have been made towards the development of quantum technologies, such as quantum computers. The prospect of a large-scale quantum computer promises breakthrough advancements in many fields, such as in the quantum simulation of materials [5, 6], as well as the ability to perform certain algorithmic tasks [7, 8] that cannot be computed with classical computers in reasonable time.

The building blocks of a quantum computer are quantum bits, also known as qubits. Over the past decades, multiple platforms for the implementation of qubits have emerged, for example trapped ions, neutral atoms, traveling photons, quantum dots or superconducting qubits. One platform that has gained significant relevance in recent years, both within academic research and industry, are superconducting qubits. A superconducting qubit is a solid state-based qubit, which is based on electrical circuits made of superconducting material. Recent advancements in the implementation of quantum error correction using the surface code architecture [9, 10] as well as bosonic encodings of quantum information [11] hint at the prospect of large-scale fault-tolerant quantum computation using superconducting qubits. Although significant advancements are still to be made and many experimental difficulties need to be solved the prospect of a large-scale fault-tolerant quantum computer using superconducting qubits is feasible in the next years or decades.

A related field of research deals with the question of how to connect distant superconducting qubits, which would allow building a quantum network of superconducting quantum computers. For example, the entanglement of distant superconducting qubits in separate dilution refrigerators separated by 30 meters via a cryogenic link has been demonstrated [12]. Such technology would be difficult to scale to larger distances and alternatives need to be developed to connect distant superconducting qubits. An alternative proposal to connect superconducting qubits is based on a microwave-to-optical quantum transducer. The idea consists of transducing the quantum information from the microwave regime, where the superconducting qubits operate, to the optical regime. This is advantageous since in the optical regime, the thermal noise is sufficiently low at room temperature, unlike in the microwave regime, where mK temperatures are needed to achieve low thermal noise. Additionally, in the optical regime, the transmission of quantum information over long distances is achievable with ultra-low loss rates [13]. Such a quantum transducer would satisfy the last two DiVincenzo criteria [14], which relate to quantum communica-

tion and quantum information. These criteria are: *the ability to interconvert stationary and flying qubits* and *the ability to faithfully transmit flying qubits between specified locations.*

Mechanical resonators are prime candidates for quantum transduction due to their ability to interface with different types of systems [15–17]. Recent work has suggested that HBARs, which are a type of mechanical resonators, are viable candidates for microwave-to-optical quantum transduction. Results in cQAD have shown coupling between superconducting qubits and the phonon modes of an HBAR [18]. Additionally, optomechanical coupling to different phonon modes of an HBAR without adding additional noise to the system, which would be crucial for a transduction protocol, has been demonstrated [4].

The quantum transduction project at the Hybrid Quantum Systems group at ETH Zurich (HYQU) aims to build a quantum transducer using an HBAR as an intermediary between the superconducting qubits and optical photons, by taking advantage of the electromechanical and optomechanical interactions that can be achieved with an HBAR. The envisioned quantum transducer consists of a qubit chip with an on-chip readout resonator flip-chip bonded to an HBAR housed inside an optical cavity, as shown in the schematics in Fig. 3.2.

Throughout this work, we focused on the design and simulation of the high-frequency transmon qubits and experimentally characterized three qubits. The need for a high-frequency transmon is due to the high Brillouin frequency of the quartz substrate of the HBAR [4], which is envisioned to be used as the substrate of the HBAR quantum transducer. **In chapter 2** we will briefly present the theoretical background needed to understand the devices that we measured. The basics of circuit quantum electrodynamics (cQED) will be discussed and the equation that describes the coupling strength between the qubit and the mechanical modes of the HBAR will be derived. In **chapter 3** the design of the high-frequency transmon qubit and the on-chip readout resonator will be explained and a proposal for a redesigned readout resonator will be presented including simulation results to tune the properties of the design. Additionally, the sensitivity of the position of the qubit chip inside the tunnel cavity will be simulated. Furthermore, we simulated the coupling strength of an $\hbar$BAR sample, which consists of the qubit chip flip-chip bonded to an HBAR made of a sapphire substrate with a pancake-shaped aluminum nitride (AlN) film patterned on top of the sapphire substrate. Finally, in **chapter 4** the experimental procedure to characterize the qubits as well as the results of the measurements of the three measured qubits will be discussed. Furthermore, the results from the measurements of the $\hbar$BAR sample will be presented.

Chapter 2

Theoretical background

In this chapter, we will briefly present the properties and necessary theoretical background of the devices simulated and measured throughout this thesis. In the first section, we discuss the basics of the transmon qubit and explain principles from cQED. In the second section, concepts from cQAD will be introduced and the equation of the electromechanical coupling strength between the electrical field from an antenna connected to a superconducting qubit and the mechanical modes of an HBAR will be derived. This equation is necessary to understand the coupling between an HBAR and a superconducting transmon qubit.

For a more comprehensive introduction to cQED we refer to [19, 20] and for a detailed derivation of the transmon qubit we refer to [21]. The work done during this thesis is partly built on previous work done at the HYQU group, specifically, the thesis work performed by Jonathan Knoll and Francesco Adinolfi [22, 23]. Those references have assisted me throughout my work and include a relevant theory section which we will partly follow in the first section of this chapter.

2.1. Circuit quantum electrodynamics

2.1.1. The transmon qubit

The transmon qubit is one of the most widely used superconducting qubits since its invention in 2007 [21]. The transmon, which was initially derived from the Cooper-pair box qubit, consists of two superconducting islands connected by a Josephson junction, as shown in Fig 2.1.b. A transmon can be made flux-tunable by connecting the superconducting islands with two Josephson junctions in parallel, also known as a superconducting quantum interference device (SQUID) [21, 24], as shown in Figure 2.1.c. In this work, we will focus on non-flux-tunable transmons.

The key element that makes the transmon a two-level system is the Josephson junction. The Josephson junction is a non-linear electronic circuit element that acts like a non-linear inductor, which makes the energy levels of the system non-equidistant, unlike a standard LC resonator. This enables the targeting of distinct energy levels, making the system an effective two-level system that can be used as a qubit. The non-equidistant energy levels of the transmon are due to the cosine potential of the transmon, which can be seen in Fig. 2.1.a.

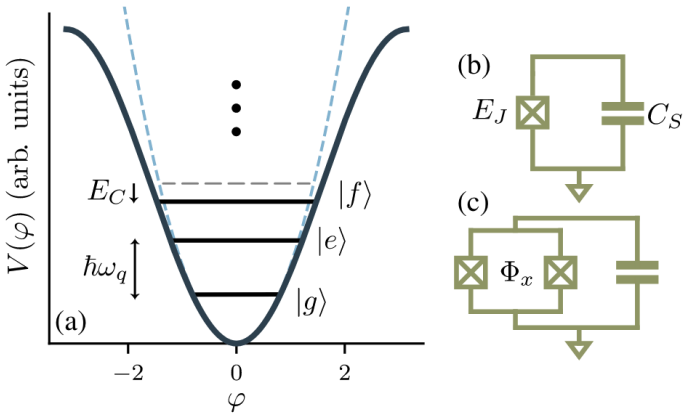

Figure 2.1.: (a) The solid line shows the cosine potential well of the transmon whereas the dashed blue line shows the quadratic potential of an LC resonator. The cosine potential gives the transmon its anharmonicity α which is approximated by $-E_C/\hbar$. (b) Circuit diagram of a fixed-frequency transmon which was used throughout this work. The circuit consists of a capacitance C_S and a Josephson junction which is represented by a square with a cross. The Josephson junction has a Josephson energy E_J and a junction capacitance of C_J. (c) Circuit diagram of a flux-tunable transmon. Here the Josephson junction is replaced by a SQUID, which consists of two Josephson junctions in parallel and allows for flux tunability of the qubit by applying an external magnetic flux Φ_x threading the SQUID loop. The figure was taken from [24].

The effective Hamiltonian that describes the transmon can be reduced to

$$\hat{H} = 4E_C(\hat{n} - n_g)^2 - E_J \cos\hat{\phi}, \tag{2.1}$$

where E_c is the charging energy, $\hat{n}$ is the charge number operator, which represents the number of Cooper pairs that tunnel between the two superconducting islands, n_g is the offset charge of the device due to external field bias, E_J is the Josephson energy and $\hat{\phi}$ is the phase operator, which can be understood as the phase difference between the two superconducting islands. For a more elaborate derivation of this Hamiltonian, we refer to [21, 24].

Note that this Hamiltonian 2.1 is also known as the Cooper-pair box Hamiltonian, which describes the Cooper-pair box qubit that predates the transmon [25]. Compared to the Cooper-pair box qubit, also known as the charge qubit, the transmon operates at a different ratio between the Josephson energy and charging energy [21, 22]. This will be explained in more detail in later parts of this section.

Given the inductance of the Josephson junction L_J, one can calculate the Josephson energy as

$$E_J = \left(\frac{\phi_0}{2\pi}\right)^2 \frac{1}{L_J}, \tag{2.2}$$

where $\phi_0 = h/2e$ is the flux quantum. The charging energy E_C is defined as

$$E_C = e^2/2C_\Sigma, \tag{2.3}$$

where $C_\Sigma = C_J + C_S$ is the total capacitance of the system consisting of the junction capacitance C_J and the shunt capacitance C_S [21].

2.1.2. The transmon regime

In the phase basis, the Hamiltonian 2.1 can be solved exactly using Mathieu functions, giving the eigenenergies

$$E_m\left(n_g\right) = E_C a_{2[n_g + k(m,n_g)]}\left(-E_J/2E_C\right), \tag{2.4}$$

where $a_v(q)$ denotes Mathieu's characteristic values and $k(m, n_g)$ is a function that sorts the eigenvalues [26].

The lowest three eigenenergies are plotted as a function of offset charge n_g in Fig. 2.2. From the Figure, it is visible that when $\frac{E_J}{E_c} \gg 1$, the difference between energy levels becomes insensitive to charge noise. When the system parameters satisfy $\frac{E_J}{E_c} \geq 50$ the qubit is said to be in the **transmon regime**.

In the transmon regime, the eigenenergies can be approximated as [21]

$$E_m \simeq -E_J + \sqrt{8E_C E_J}\left(m + \frac{1}{2}\right) - \frac{E_C}{12}\left(6m^2 + 6m + 3\right), \tag{2.5}$$

where $\omega_p = \sqrt{8E_C E_J}/\hbar$ is the Josephson plasma frequency. From Eq. 2.5, the qubit frequency, which is the frequency difference between the ground state and the first excited state, can be approximated to

$$\hbar\omega_{10} \approx \sqrt{8E_C E_J} - E_C. \tag{2.6}$$

An important quantity when designing the transmon is the anharmonicity, which is defined as follows

$$\alpha = \omega_{12} - \omega_{01} = \frac{(E_{12} - E_{01})}{\hbar} \approx -\frac{E_C}{\hbar}, \tag{2.7}$$

where E_{01}, ω_{01} is the energy transition and frequency difference respectively, between the ground state and the first excited state. E_{12}, ω_{12} is the energy transition and frequency difference respectively, between the first and second excited excited state. The last approximation is made using Eq. 2.5.

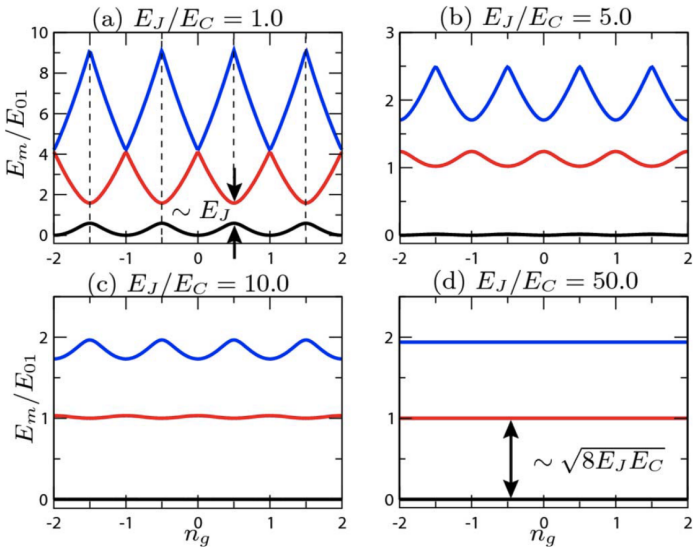

Figure 2.2.: Eigenenergies E_m of the transmon Hamiltonian as a function of the offset charge n_g in units of the energy levels, for different ratios of $\frac{E_J}{E_c}$. The figure was taken from [21].

2.1.3. Control and interaction with a qubit

The concepts and ideas to control a system in circuit quantum electrodynamics (cQED) are based on cavity quantum electrodynamics (CQED) [19, 23]. In CQED the qubit is an atomic system, for example, an atom or an ion, which is typically confined in an optical cavity. Lasers are then used to manipulate, control and readout the state of the qubit. Similarly, in cQED the superconducting qubit takes the role of the atom, for example a transmon superconducting qubit, and the optical cavity is replaced by a superconducting readout resonator. The state of the qubit can then be controlled and manipulated using microwave pulses that are sent via transmission lines to the system. Typically, to perform measurements, our device needs to be in the **strong coupling regime** [24, 27] $g \gg \kappa, \gamma$, where κ is the linewidth of the readout resonator and γ is the linewidth of the qubit.

The Jaynes-Cummings Hamiltonian is used to describe the interaction in a qubit-resonator system [20]

$$H_{\mathrm{JC}} = \hbar\omega_r \left(a^\dagger a + \frac{1}{2}\right) + \frac{\hbar\omega_{\mathrm{q}}}{2}\sigma_z + \hbar g \left(\sigma_+ a + \sigma_- a^\dagger\right), \tag{2.8}$$

where ω_r is the resonator frequency, ω_q is the qubit frequency, g is the coupling strength between the qubit and the resonator, the operators a and $a^\dagger$ represent the annihilation and excitation operators of the resonator, whereas σ_- and σ_+ are the same operators for the qubit.

Generally, the coupling strength g between the readout resonator and the qubit is proportional to the overlap integral between the dipole moment of the qubit $\vec{d}_{qubit}$ and Electric field $\vec{E}_{res}$ of the readout resonator:

$$g \propto \int \vec{d}_{qubit} \cdot \vec{E}_{res}. \tag{2.9}$$

Note that the electric field is inversely proportional to the square root of the capacitance and inductance of the readout resonator, and therefore decreases as we increase the capacitance or inductance of the system [24]. This property will play an important role when redesigning the qubit, which will be shown in subsection 3.3 of the next chapter.

2.1.4. The dispersive regime

When the detuning $\Delta = w_q - \omega_r$ is large compared to the coupling rate g, $\Delta \gg g$, the system is said to be in the **dispersive regime**. In this regime, the direct exchange of excitations between the qubit and the resonator is suppressed [24] and the Hamiltonian in Eq. 2.8 can be approximated to the **dispersive Hamiltonian**

$$H_{\mathrm{disp}} = \hbar \left(\omega_r' + \frac{\chi\sigma_z}{2}\right) \left(a^\dagger a + \frac{1}{2}\right) + \frac{\hbar\omega_q'}{2}\sigma_z, \tag{2.10}$$

where χ is the qubit-state-dependent dispersive cavity shift and σ_z is a Pauli operator. The frequencies $\omega_r' = \omega_r - \frac{g^2}{\Delta - E_C/\hbar}$ and $\omega_q' = \omega_q + \frac{g^2}{\Delta}$ are the dressed readout resonator and qubit frequencies, which are the frequencies that can be measured experimentally in the dispersive regime. Note that ω_r and ω_q are the bare frequencies of the readout resonator and the qubit. For the derivation of the dispersive Hamiltonian we refer to Ref. [19, 24]. The dispersive shift is given by

$$\chi = -\frac{2g^2 E_C/\hbar}{\Delta(\Delta - E_C/\hbar)} \approx -\frac{2g^2\alpha}{\Delta(\Delta - \alpha)}, \tag{2.11}$$

where the second approximation $\alpha \approx E_C/\hbar$ is valid when we are in the transmon regime. From the dispersive Hamiltonian in Eq. 2.10 one can see that the qubit induces a shift by χ to the resonator frequency depending on whether the qubit is in the excited or ground state. This is the mechanism used to readout the state of the qubit, known as the dispersive readout. Specifically to readout the state of the qubit, we can probe the readout resonator on resonance in transmission. When the qubit is in the excited state, the transmission signal will decrease since the frequency of the readout resonator shifts by χ. To perform this readout the **strong dispersive limit** condition $\chi \gg \kappa, \gamma$, must be fulfilled. Alternatively to the readout in transmission, one can also perform the readout in phase.

2.1.5. Purcell effect

Due to the coupling between the transmon and the cavity, the qubit experiences an increased decay rate. This can be explained by the hybridization of the qubit mode and the cavity mode. Since the cavity mode decays with a rate κ and the qubit mode is hybridized with the cavity mode, the qubit has an increased decay rate since it can decay via the cavity. This effect is known as the **Purcell effect**.

In the context of our transmon cavity system, when we are in the dispersive regime $\Delta \gg g$ the qubit decay rate γ_κ due to the Purcell effect is given by

$$\gamma_\kappa = \left(\frac{g}{\Delta}\right)^2 \kappa. \tag{2.12}$$

2.2. Coupling to a high-overtone bulk acoustic resonator

Throughout this thesis, we measured and simulated the coupling between the electrical field of a high-frequency superconducting transmon qubit and the acoustic phonon modes of an HBAR. This coupling between the transmon is mediated via a thin film of a piezoelectric material, typically made out of AlN, which is patterned on top of the non-piezoelectric substrate of the HBAR, such as sapphire or quartz. The two chips are later flip-chip bonded. Such devices have previously been measured [2, 18, 28, 29]. The design will be further explained in the next chapter of this thesis in section 3.1. In this section, we will briefly describe the basic properties of an HBAR as well as derive an expression for the electromechanical coupling between the transmon and the HBAR.

2.2.1. High-overtone bulk acoustic resonator

The hybrid electromechanical system consists of an HBAR, where the surfaces of the substrate and the pancake-shaped or dome-shaped AlN film form a phononic Fabry-Perot resonator, which supports transversely polarized and longitudinally polarized mechanical modes [18]. In Fig. 2.3 we show a pancake-shaped HBAR.

The acoustic wavelength of the phonon modes in the HBAR is much smaller than the diameter of the pancake-shaped AlN film, therefore the acoustic wave does not diffract significantly and thereby forms a confined mode in the HBAR which is thus long-lived [18].

The HBAR consisting of a pancake-shaped AlN film patterned on top of the substrate of the HBAR, as shown in Fig. 2.3, forms a cylinder-shaped mode volume. The strain field profile, normalized to one photon, of the modes in a cylinder-shaped mode volume can be described by

$$S_{l,m}(\vec{x}) = \beta_{l,m} \sin\left(\frac{l\pi z}{h}\right) J_0\left(\frac{2j_{0,m}r}{d}\right), \tag{2.13}$$

where J_0 is the 0-th order Bessel function of the first type, $j_{0,m}$ is the m^{th} root of J_0, h is the height of the substrate, d is the diameter of the pancake-shaped cylindrical AlN film and $\beta_{l,m}$ is the normalization factor that guarantees that the total energy of the phonon mode is $\hbar\omega_{phonon}$ [18]. The indices l and m are the longitudinal and transverse mode indices.

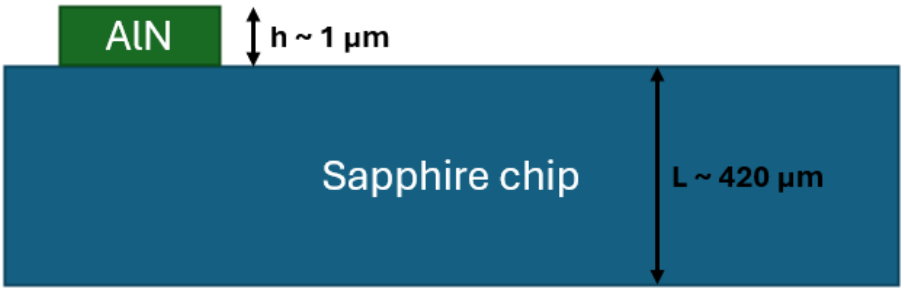

Figure 2.3.: Schematics of the HBAR consisting of a sapphire substrate and a piezoelectric pancake-shaped AlN film patterned on top of the substrate. The acoustic waves are confined in the region under the pancake. The diameter of the pancake-shaped AlN film of the HBAR that was measured in this work is 400 μm. The results of the measurements with this HBAR will be discussed in section 4.3.

The expected frequency of the modes is given by

$$\omega_{l,m} = \sqrt{\left(\frac{l\pi}{h}\right)^2 v_l^2 + \left(\frac{2j_{0,m}}{d}\right)^2 v_t^2}, \tag{2.14}$$

where v_l and v_t are the longitudinal and effective transverse sound velocities respectively.

2.2.2. Electromechanical coupling

In this subsection, we will derive the single photon coupling strength between an arbitrary electric field along the z-direction and a strain field with an arbitrary transverse profile. For the derivation of the coupling strength, I follow the Supplementary material [18] as well as previous calculations made by Tom Schatteburg. The general expression for the interaction Hamiltonian between the qubit and the phonon mode of a HBAR is given by

$$H = -\int \sigma(\vec{x}) S(\vec{x}) dV, \tag{2.15}$$

where $\sigma(\vec{x})$ is the stress tensor that is generated via the piezoelectricity of the AlN film due to the electric field $E(\vec{x})$ from the antenna of the transmon. The stress tensor acts on the strain field $S(\vec{x})$ of the phonon modes of the HBAR. The integration is performed over the volume of the piezoelectric AlN film of the HBAR since the interaction is mediated via the piezoelectricity of the piezo.

Typically, one considers only the dominant tensor component which in our case is along the longitudinal direction that is perpendicular to the surface of the substrate of the HBAR. This direction is denoted with the subscript 3 in the following expression. Using this consideration as well as the expression for the stress tensor along the 33 direction $\sigma(\vec{x}) = c_{33}^p d_{33}^p E(\vec{x})$, we arrive at the following equation for the interaction Hamiltonian

$$H_{\text{int}} = -c_{33}^p d_{33}^p \int_{V_{piezo}} E_z(x,y,z) S_z(x,y,z) dV, \tag{2.16}$$

where c_{33}^p and d_{33}^p are the stiffness and piezoelectric tensor components of the piezoelectric material. Note that we assume that the electric field $E_z(x,y,z)$ is constant along the small thickness of the piezo, defined as the z-direction and we can quantize the qubit mode such that $E_z(x,y,z) = E_z(x,y)\left(a + a^\dagger\right)$.

The general expression for a strain field of a mode with an arbitrary transverse profile $f(x,y)$ can be written as

$$S_z(\vec{r},t) = S_{0,z} f(x,y) \sin(k(z)z) \left(be^{-i\omega t} + b^\dagger e^{+i\omega t}\right), \tag{2.17}$$

where $S_{0,z}$ is the strain field of the zero-point fluctuations, $f(x,y)$ is the transverse mechanical mode profile, b and $b^\dagger$ represent the annihilation and excitation operators of the phonons in the HBAR and ω is the frequency of the mechanical mode. The z-dependence of the mechanical mode is represented by the term $\sin(k(z)\cdot z)$. Note that the z-dependence of the wavenumber k stems from the fact that the HBAR consists of two materials, namely sapphire and a piezoelectric AlN material, which have different sound velocities due to the different material properties. This will play an important role in the next subsection 2.2.3 where we will integrate $S_z(\vec{r},t)$ over the volume of the HBAR. Furthermore, we assume that the transverse profile $f(x,y)$ is approximately constant along the thickness of the HBAR because the envelope of the field is slowly varying. Note that the transverse mode profile $f(x,y)$ is normalized such that $\iint_{xy} |f(x,y)|^2 dxdy = 1$.

In subsection 2.2.3, we will derive the normalization constant $S_{0,z}$ for the strain field to have the energy of one phonon. By inserting Eq. 2.17 into 2.16 we arrive at the following expression for the interaction Hamiltonian

$$\begin{aligned} H_{\text{int}} &= -e_{33}^p S_{0,z} \int E_z(x,y) f(x,y) \sin(k_p z)\, dV \left(ab + a^\dagger b + ab^\dagger + a^\dagger b^\dagger\right) \\ &= -e_{33}^p S_{0,z} \int E_z(x,y) f(x,y) \sin(k_p z)\, dV \left(a^\dagger b + ab^\dagger\right), \end{aligned} \tag{2.18}$$

where $e_{33}^p = c_{33}^p d_{33}^p$. Note that we used the rotating wave approximation (RWA) in the second inequality.

This interaction Hamiltonian can be equated to the Jaynes-Cummings Hamiltonian

$$H_{\text{int}} = -\hbar g \left(a b^\dagger + a^\dagger b \right), \tag{2.19}$$

where g is the coupling strength between the qubit and the phonon mode. By equating Eq.2.18 and 2.19, an expression for the coupling strength can be calculated as

$$\begin{aligned} \hbar g &= -e_{33}^p S_{0,z} \int E_z(x,y) f(x,y) \sin(k_p z)\, dV \\ &= -e_{33}^p S_{0,z} \iint_{xy} E_z(x,y) f(x,y) dx dy \int_z \sin(k_p z)\, dz. \end{aligned} \tag{2.20}$$

After evaluating the integral over the thickness of the piezo d_p and plugging in the expression for the normalization constant $S_{0,z} = \sqrt{\frac{\hbar\omega}{\left(c_{33}^p d_p + c_{33}^s d_s\right)}}$ that ensures that the strain field will have the energy of one phonon as we will show in subsection 2.2.3, we calculate the coupling strength

$$\hbar g = v_p e_{33}^p \sqrt{\frac{\hbar}{\omega \left(c_{33}^p d_p + c_{33}^s d_s\right)}} \left(1 - \cos\left(\frac{\omega}{v_p} d_p\right)\right) \int_{x,y} E_z(x,y) f(x,y) dx dy. \tag{2.21}$$

In the next chapter of this report, we will utilize Eq.2.21 to calculate the coupling strength between the electric field $E_z(x,y)$ from the qubit antenna and the transverse mode profile $f(x,y)$ of the mechanical modes of the HBAR.

2.2.3. Normalized strain field

We want to derive the strain field of the HBAR of an arbitrary transverse mode profile. For the derivation, we assume that the transverse mode profile over the length of the crystal is constant. The HBAR consists of a piezoelectric film of thickness d_p patterned on top of a crystalline substrate of thickness d_s.

The real strain field along the z-direction is given by

$$S_z(\vec{r}, t) = S_{0,z} f(x,y) \sin(k(z) \cdot z) \left(b e^{-i\omega t} + b^\dagger e^{+i\omega t} \right). \tag{2.22}$$

The real strain field is normalized such that

$$\langle H \rangle = \int_V \frac{c_{33}}{2} \left| S_z(\vec{r}, t) \right|^2 dV = \frac{\hbar\omega}{2} + \bar{n}\hbar\omega, \tag{2.23}$$

where c_{33}^p is the stiffness tensor in the 33 direction, $\frac{\hbar\omega}{2}$ is the rest point energy and $\bar{n}$ is the average number of phonons in the HBAR. Note that the integration here is performed over the entire HBAR consisting of an AlN piezoelectric film and a substrate.

The second equality implies the normalization of the strain field, where the energy stored in the HBAR consists of $\frac{\hbar\omega}{2}$, which is the rest point energy, and $\bar{n}\hbar\omega$, which is the energy contribution from the number of phonons in the HBAR.

The energy $\langle H \rangle$ can be calculated by plugging Eq.2.22 into Eq.2.23 and performing the RWA and evaluating the integral. This yields the following expression for the energy:

$$\begin{aligned}
\langle H \rangle &= 2 \int_V \frac{c_{33}}{2} \left| S_z(\vec{r}, t) \right|^2 dV \\
&= S_{0,z}^2 \left\langle b^\dagger b + b b^\dagger + b b e^{-2i\omega t} + b^\dagger b^\dagger e^{2i\omega t} \right\rangle \int_{-\infty}^{\infty} \int_{-\infty}^{\infty} |f(x,y)|^2 dx dy \\
&\quad \cdot \left(\int_0^{d_p} c_{33}^p \sin^2\left(k_p z\right) dz + \int_0^{ds} c_{33}^s \sin^2\left(k_s z + k_p d_p\right) dz \right) \\
&= S_{0,z}^2 \left\langle 2 b^\dagger b + 1 \right\rangle \cdot \\
&\quad \cdot \left(c_{33}^p \int_0^{d_p} \left(\frac{1}{2} - \cos\left(\frac{2 k_p z}{2} \right) \right) dz + c_{33}^s \int_0^{ds} \left(\frac{1}{2} - \frac{\cos\left(2\left(k_s z + k_p d_p\right)\right)}{2} \right) dz \right) \\
&= (2\bar{n} + 1) S_{0,z}^2 \left(c_{33}^p \left[\frac{z}{2} - \frac{\sin\left(2 k_p z\right)}{4 k_p} \right]_0^{d_p} + c_{33}^s \left[\frac{z}{2} - \frac{\sin\left(2\left(k_s z + k_p d_p\right)\right)}{4 k_3} \right]_0^{ds} \right) \\
&= (2\bar{n} + 1) S_{0,z}^2 \left(c_{33}^p \frac{d_p}{2} + c_{33}^s \frac{ds}{2} + \sin\left(2 k_p d_p\right) \left(- \frac{c_{33}^p}{4 k_p} + \frac{c_{33}^s}{4 k_s} \right) \right).
\end{aligned} \tag{2.24}$$

In the first equality, there is a factor 2 because the energy consists of both kinetic and potential energy. In the second equality, we plug in Eq. 2.22 and integrate over the transverse (x, y) direction of the HBAR. Note that for the integration along the z-direction, we separate the integration between the piezoelectric section of the HBAR and the substrate section of the hbar. In the third equality, we use the normalization of the transverse mode profile $\int_{-\infty}^{\infty} \int_{-\infty}^{\infty} |f(x,y)|^2 dx dy = 1$ and the trigonometric identity $\sin(\phi) = \frac{1}{2}\cos(2\phi)$ to simplify the expression. Furthermore, we perform the RWA which neglects rapidly rotating terms, therefore $b b e^{-2i\omega t} = 0$ and $b^\dagger b^\dagger e^{2i\omega t} = 0$. In the fourth inequality, we use $\left\langle b^\dagger b \right\rangle = \bar{n}$ where $\bar{n}$ is the mean phonon number in the HBAR and calculate the definite integral. In the last inequality, we evaluate the integral and utilize the resonance-matching condition

$$k_s d_s + k_p d_p = m \cdot \pi \Rightarrow \sin\left(2\left(k_s d_s + k_p d_p\right)\right) = 0, \tag{2.25}$$

where m is an integer.

To further simplify Eq. 2.24, we will focus on the expression in the brackets, which can be approximated by

$$\begin{aligned} & c_{33}^{p}\frac{d_p}{2}+c_{33}^{s}\frac{d_s}{2}+\sin\left(2k_pd_p\right)\left(-\frac{c_{33}^{p}}{4k_p}+\frac{c_{33}^{s}}{4k_s}\right) \\ & =c_{33}^{p}\frac{d_p}{2}+c_{33}^{s}\frac{d_s}{2}+\frac{\sin\left(2k_pd_p\right)}{4\cdot 2\pi}\left(-c_{33}^{p}\lambda_p+c_{33}^{s}\lambda_s\right) \\ & \approx c_{33}^{p}\frac{d_p}{2}+c_{33}^{s}\frac{d_s}{2}, \end{aligned} \tag{2.26}$$

where in the first equality we use the relation between the wavelength λ and the wavenumber $k = 2\pi/\lambda$. When fabricating the HBAR we often aim for optimal coupling $d_p = \frac{\lambda_p}{2}$ such that the third term containing the expression $\sin(2k_pd_p)$ will vanish. However, even if we are not close to optimal coupling, the main contribution comes from the term $c_{33}^{s}\frac{d_s}{2}$ since $d_s \gg d_p$ and $\frac{d_s}{2} \gg \lambda_p, \lambda_p$. For the following calculation, we will also keep the term $c_{33}^{p}\frac{d_p}{2}$.

This yields the following expression for the energy

$$\langle H\rangle = (\bar{n}+1/2)S_{0,z}\left(c_{33}^{p}d_p+c_{33}^{s}d_s\right). \tag{2.27}$$

As explained above, the energy in the HBAR can also be given by

$$\langle H\rangle \stackrel{!}{=} \frac{\hbar\omega}{2}+\bar{n}\hbar\omega. \tag{2.28}$$

By equating equations 2.27 and 2.28 we can arrive at an expression for the $S_{0,z}$:

$$S_{0,z} = \sqrt{\frac{\hbar\omega}{\left(c_{33}^{p}d_p+c_{33}^{s}d_s\right)}}. \tag{2.29}$$

Finally, by plugging Eq.2.29 into 2.22 we arrive at the final expression for the strain field along the z-direction

$$S_z(\vec{r},t) = \sqrt{\frac{\hbar\omega}{\left(c_{33}^{p}d_p+c_{33}^{s}d_s\right)}}f(x,y)\sin(k(z)z)\left(be^{-i\omega t}+b^{\dagger}e^{+i\omega t}\right). \tag{2.30}$$

Chapter 3

Design and simulations

Before fabrication and measurements, the devices are simulated using the finite-element electromagnetic eigenmode simulation software Ansys HFSS. In this chapter, we will present the design properties and selected simulation results of the devices measured throughout this work. Previous versions of the high-frequency transmon were initially designed by Francesco Adinolfi [23] and further adjustments have been made by members of the HYQU group, primarily by Tom Schatteburg.

Simulations of the device are initially performed using Ansys. Since the Josephson junction, which is at the core of the transmon qubit, is a nonlinear element that can only be modeled as a linear inductor by Ansys, we further use the python energy-participation ratio package (pyEPR) [30] software package which can model the non-linearity of the Josephson junction. The code that we used throughout the thesis to perform automated simulations with Ansys and pyEPR was developed by members of the HYQU group and automatized in the thesis work of Jonathan Knoll [22].

In the first section, we will present the design of the high-frequency transmon and the on-chip readout resonator and briefly show the envisioned design of the quantum transducer. In the second section, the sensitivity of the qubit chip positioning inside the tunnel cavity will be simulated and discussed. Furthermore, a redesign of the readout resonator will be presented in the third section of this chapter, including simulation results and an explanation of the design process performed to reach the ideal design parameters for the device. Lastly, we will present simulations of the electromechanical coupling strength between the electric field from the qubit antenna and the mechanical modes of the HBAR for a device that was measured throughout this work.

3.1. Design of the qubit and readout resonator

3.1.1. Qubit geometry

The non-flux-tunable qubit that we utilized throughout this work consists of two superconducting pads connected by a Josephson junction, as shown in Figure 3.1. The transmon is fabricated using standard fabrication techniques. Compared to standard qubit geometries, our design has an additional antenna connected to the right qubit pad. This antenna is necessary to interact efficiently with mechanical modes of the HBAR, a similar design is shown in Ref. [2] and [28]. The size of the antenna is larger compared to previous cQAD experiments [28]. This is because the laser beam must fit through the antenna as shown in Figure 3.2. The clipping of the beam is undesirable, therefore the antenna has to be chosen sufficiently large. This will be explained more precisely when discussing the envisioned design of the quantum transducer in subsection 3.1.2.

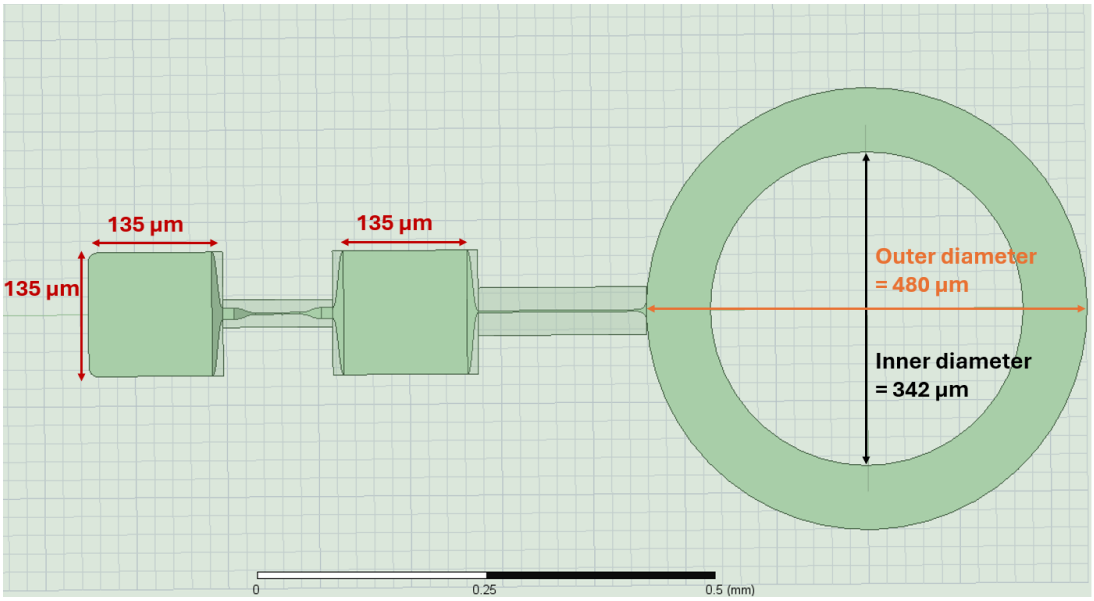

Figure 3.1.: Zoomed in picture of the qubit chip showing the qubit geometry including some key parameters. The qubit consists of two superconducting islands, connected by a Josephson junction. The right qubit pad is extended by a qubit antenna, thereby increasing its capacitance. The electric field from the antenna is used to electromechanically interact with an HBAR, which will be flip-chip bonded to the qubit chip.

To tune the frequency of the qubit, the Josephson energy E_J, and the charging energy E_C are changed such that a desirable frequency is reached according to Eq. 2.6. The initial design of the qubit to achieve a higher transmon frequency started with a qubit design in

the normal cQED frequency range of about 4-8 GHz. To increase the frequency, both E_J and E_C were increased while preserving the condition for the transmon regime $\frac{E_J}{E_c} \geq 50$. To increase E_J, the Josephson junction inductance L_J is decreased, according to Eq. 2.2 which describes the relation between E_J and L_J. To increase E_C the capacitance of the system is decreased by decreasing the size of the superconducting capacitor pads, this can be understood from Eq. 2.3. The first simulations to target the higher qubit frequencies while maintaining the transmon regime condition were done by Francesco Adinolfi [23] and were later adjusted by Tom Schatteburg.

It is important to note that the capacitance of the antenna also plays an important role in this design since it is much larger than the antenna used in previous work where an antenna is used to interact with the mechanical modes of an HBAR [2].

3.1.2. The HBAR quantum transducer

A sketch of the quantum transducer is shown in Fig. 3.2. The envisioned transducer consists of a high-frequency superconducting qubit flip-chip bonded to an HBAR consisting of a quartz substrate and an AlN film patterned on top of the substrate. An excitation of the qubit can be swapped into an excitation of a phonon of the HBAR via the electromechanical coupling. To swap the phononic excitation of the mechanical mode of the HBAR into the optical regime, the optomechanical interaction between the HBAR and the light inside the optical cavity, as shown in Fig. 3.2, is utilized.

From this design, we can understand that the size of the antenna is crucial for the quantum transducer to work since it must be large enough for the laser beam to pass through it without being clipped by the antenna. The envisioned transducer consists of an HBAR with a quartz substrate because the Brillouin frequency, which determines at what frequency we can optomechanically interact with the HBAR, is much lower for quartz than sapphire, which is typically used as the substrate of the HBAR. For the transduction protocol to work, the frequency of the qubit should match the Brillouin frequency. The Brillouin frequency of quartz is 12.65 GHz [4], for optical light at 1550 nm, which is the reason why this work focuses on the development of a high-frequency transmon.

The preliminary design of the quantum transducer is shown in Fig. 3.3. In the inset of the Figure, we can see that the qubit chip, which is flip-chip bonded to the HBAR chip, is housed inside a tunnel cavity. In Fig. 3.4 the simulation setup of the inner part of the tunnel cavity, in which the qubit and HBAR chips are housed, is shown. The measurement and control of the qubit are performed in transmission via the output and input pins. The qubit chip consists of a transmon qubit with a large antenna as well as an on-chip readout resonator used to dispersively readout the state of the qubit as described in section 2.1.4.

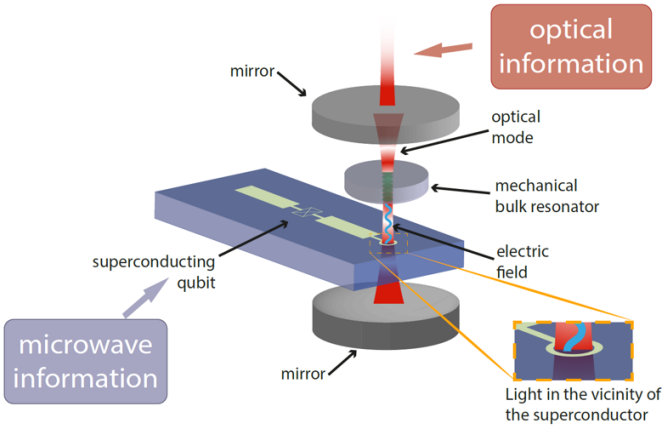

Figure 3.2.: Schematics of the HBAR microwave-to-optical quantum transducer. The electric field that emanates from the qubit antenna is used to electromechanically interact with the HBAR resonator, such that an excitation in the qubit can be swapped into a phononic excitation of the HBAR. Finally, a laser is used to optomechanically interact with the mechanical modes of the HBAR to swap the excitation to the optical regime. The figure was taken from a poster presentation by Dr. Rodrigo Benevides from the HYQU group.

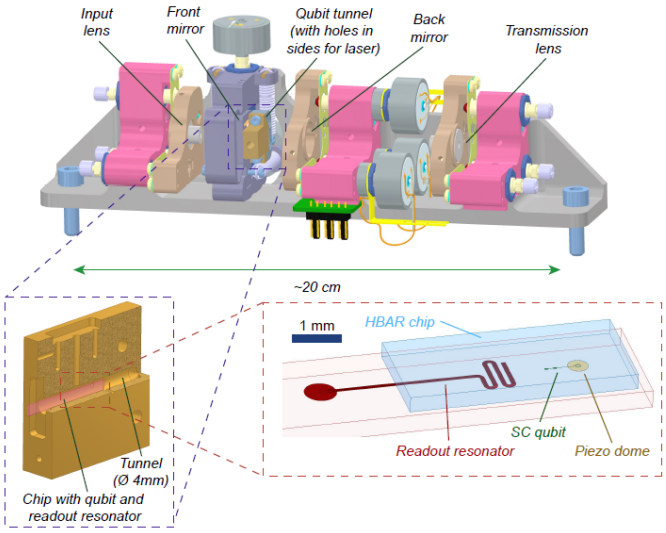

Figure 3.3.: Image of a preliminary schematics of the HBAR transducer. The image was taken from a poster presentation by Hugo Doeleman from the HYQU group.

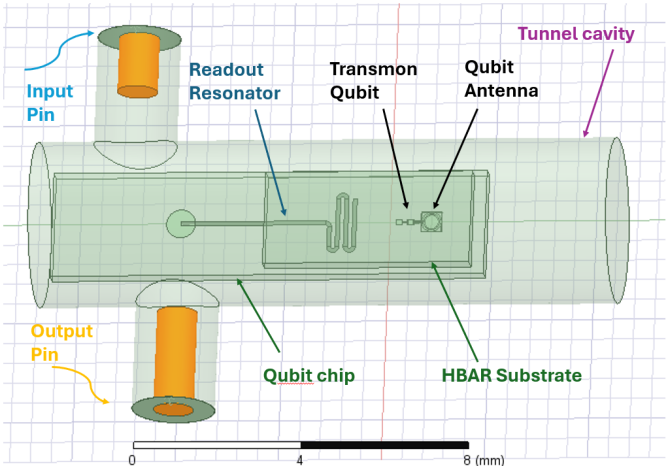

Figure 3.4.: Simulation setup of the inner part of tunnel cavity in which the qubit and HBAR chips are housed. Control and readout of the device are performed via the input and output pins. Note that for this tunnel cavity, the readout is performed in transmission.

3.2. Sensitivity of the chip positioning in the tunnel cavity

As explained in the previous subsection, the qubit chip is housed inside a tunnel cavity where it is suspended on the left side of the tunnel. This means that the majority of the qubit chip is not attached to any part of the tunnel and is therefore similar to a suspended cantilever. Due to possible vibrations of the dilution refrigerator or other experimental effects, it is possible that the qubit chip is vibrating and that its position is not fixed between measurements. We suspected that this could change the properties of the device. For example, the qubit frequency w_q, the coupling strength between the qubit and the readout resonator g and thereby also the dispersive shift χ, could be affected. To test this hypothesis, we can simulate the sensitivity of those properties with respect to a change in the position of the qubit chip inside the tunnel cavity. This can be done by sweeping the position of the qubit chip around its expected position in different directions and performing Ansys simulations and pyEPR analysis for every variation of the sweep. Note that pyEPR has two different versions of calculating frequencies, namely a method based on numerical diagonalization (which is denoted with the subscript **ND**) and a method based on first-order perturbation theory (which will be denoted with the subscript **O1**). For the simulations performed in this subsection, I used the numerical diagonalization method. This choice was made because the dispersive shift χ was predicted more precisely by this method when we compared it to the measurements for the first device that we measured as shown in table 4.1 of the next chapter.

In Fig. 3.5 the variables that are varied to test the sensitivity of the qubit are defined. The variables **chip_q_x_offset**, **chip_q_z_offset** and **qubit_wall_spacing** in the figure can be changed to move the qubit chip in the x, z and y-position respectively. The variable **chip_offset_special** can be tuned to increase the tunnel cavity length.

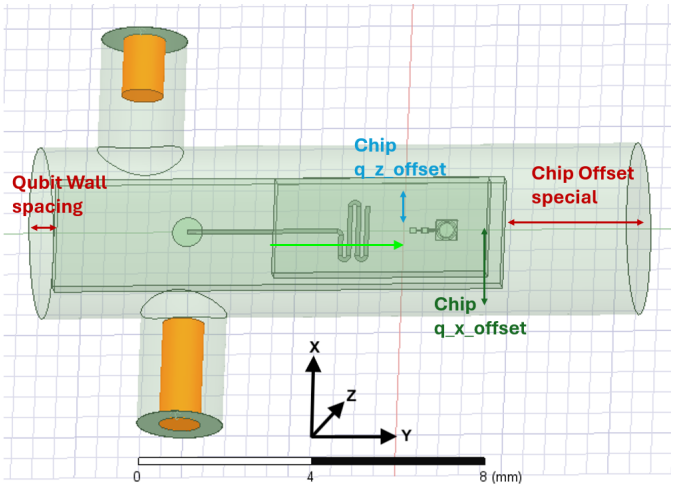

Figure 3.5.: Relevant parameters for changing the position of the qubit chip inside the resonator. The variable **chip_q_z_offset** changes the z-position of the qubit, which is perpendicular to the qubit chip. The variable **chip_q_x_offset** changes the x-position of the qubit chip which is in the plane of the qubit chip. The variable **Qubit wall spacing** changes the y-position of the qubit chip, which is in the plane of the qubit chip and parallel to the cylinder axis of the tunnel cavity. Lastly, the **chip_offset_special** increases the length of the tunnel cavity.

3.2.1. Simulations of the sensitivity of the qubit chip positioning

As shown in Fig. 3.6 the detuning Δ and the coupling strength g are relatively insensitive to changes in the x-position of the qubit chip. From the plots we can see that both Δ and g vary by less than 5 % as we change the x-position of the chip by up to 0.4 mm around the standard center position. As expected, we can see a symmetric pattern around the standard chip position where the chip_q_x_offset is set to 0 mm. This is especially visible when observing the change of g as seen in Fig. 3.6b.

The results of the sweep of the z-position of the qubit chip are shown in Fig. 3.7. Both the detuning Δ and the coupling strength g are relatively insensitive to the z-position. Similarly, the results of the sweep of the y-position of the qubit chip, by sweeping the variable qubit_wall_spacing, are shown in Fig. 3.8. The frequency variation shown in Fig. 3.8a when changing the z-position by 0.2 mm around the standard qubit chip

position (where the qubit wall spacing is 0.3 mm) is smaller than 2 %. For the coupling strength we see a more significant change as shown in Fig. 3.8b where the coupling strength decreases as we increase the qubit_wall_spacing. A possible explanation for this behavior is that when the qubit chip is closer to the tunnel cavity wall, the field of the qubit can change due to the vicinity of the wall. Therefore, the dipole of the qubit as seen by the readout resonator can be reduced, which would explain the reduced coupling strength according to Eq. 2.9. This result led us to test whether the length of the tunnel cavity also changes the coupling strength. The results are shown in the next subsection 3.2.2.

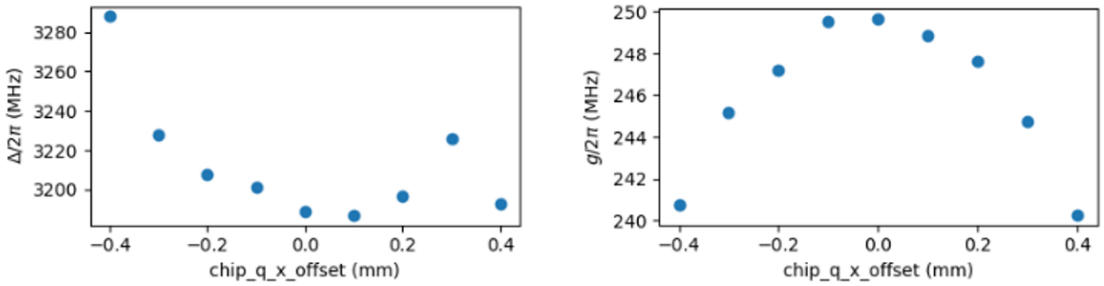

a b

Figure 3.6.: Detuning Δ (subplot **a**) and coupling strength g (subplot **a**) between the qubit and the readout resonator for different x-positions of the qubit chip.

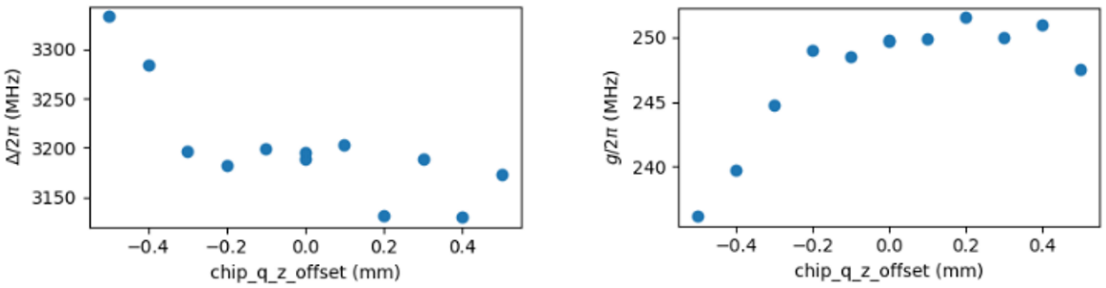

a b

Figure 3.7.: Detuning Δ (subplot **a**) and coupling strength g (subplot **b**) between the qubit and the readout resonator for different z-positions of the qubit chip.

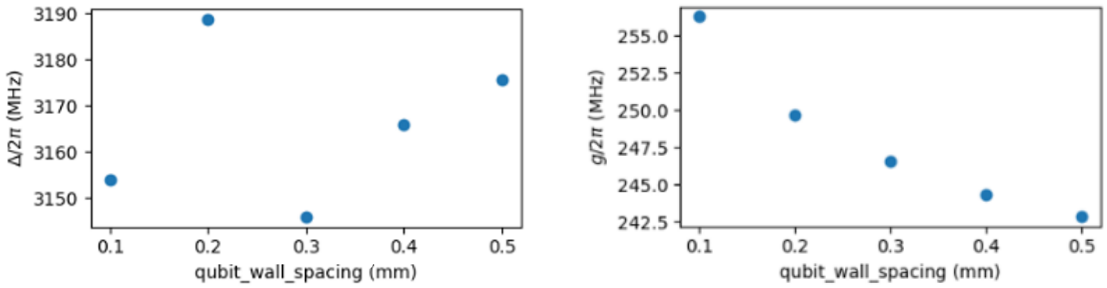

a b

Figure 3.8.: Detuning Δ (subplot **a**) and coupling strength g (subplot **a**) between the qubit and the readout resonator for different y-positions of the qubit chip. Note that the standard chip position is when **qubit_wall_spacing** is equal to 0.3 mm.

3.2.2. Sweeping the tunnel cavity length

Fig. 3.9 shows a plot of the coupling strength g vs the chip_offset_special variable, with which the length of the tunnel cavity can be controlled. As expected, one can see a similar behavior as in Fig. 3.8b where, as the tunnel length increases the coupling strength decreases. Since we do not want the coupling strength to be influenced by the distance between the qubit chip and the end of the tunnel cavity, we change the length of the tunnel cavity to a regime where the coupling strength does not vary significantly. In Fig. 3.9 we see that as we increase the length of the cavity the variation of the coupling strength becomes smaller, which is desirable for a more reliable prediction of the measurement results. Therefore the length of a second cavity which was produced and used for measurements was adjusted to a value of the chip_offset_special of 3 mm.

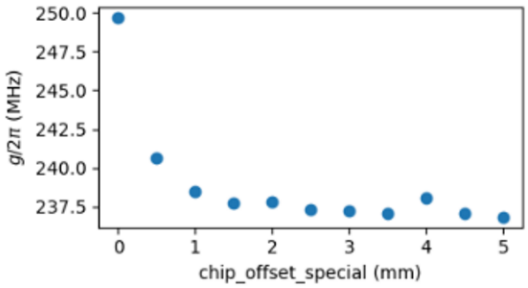

Figure 3.9.: Coupling strength g between the qubit and the readout resonator when sweeping the length of the tunnel cavity. The variable **chip_offset_special** practically increases the length of the cavity as explained in 3.5.

3.3. Redesign of the readout resonator

The initial design of the readout resonator can be seen in Fig. 3.4. Since the process of tuning the device parameters to reach the targeted device properties, such as the readout resonator frequency ω_r, coupling strength g and dispersive shift χ, is time-consuming, we propose a new design of the readout resonator to optimize the tuning process of the device. The specific goal is to redesign the readout resonator such that the coupling strength can be adjusted while only slightly changing the readout resonator frequency. Compared to the initial design, the redesign of the readout resonator includes an additional resonator lead that points to the left capacitor pad of the qubit, as shown in Fig. 3.10. The purpose of this is that the coupling strength g between the qubit and the readout resonator will be primarily controlled via the length of this resonator lead. This should be the case since the overlap between the field of the readout resonator as seen by the qubit, and the dipole moment of the qubit, is proportional to g according to Eq. 2.9. This overlap is expected to be largest in the area of the resonator lead part due to its proximity to the left qubit pad and therefore we could tune g using the resonator lead part.

To study this design, we perform sweeps of the parameters defined in 3.10 and perform Ansys and pyEPR simulations to obtain the device properties for each instance of the sweep. To achieve the desired readout resonator frequency and dispersive shift χ, we iteratively sweep the parameters **resonator meander length**, **conductor width**, and **resonator to qubit length** to the qubit. For the simulations performed in this subsection, unless stated otherwise in the title of a figure, we chose the pyEPR simulation method based on numerical diagonalization.

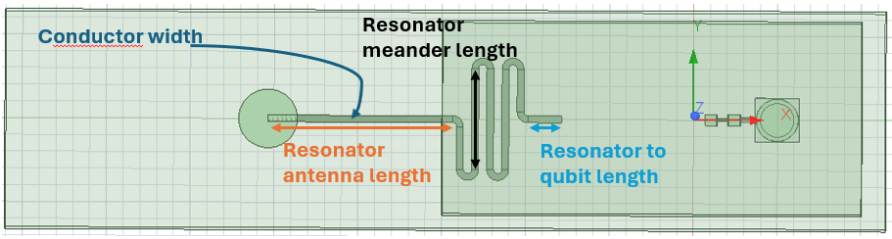

Figure 3.10.: Image of the qubit chip including the redesigned on-chip readout resonator. The parameters which control the design of the readout resonator are defined in the image. To reach an optimal design, we perform sweeps of these parameters and for each instance of the sweep the relevant properties, such as the readout resonator frequency ω_r, coupling strength g and dispersive shift χ, are calculated using Ansys and pyEPR.

In the left plot of Fig. 3.11 we see that the frequency of the readout resonator ω_r slightly decreases, as we increase the parameter resonator to qubit length. This effect is expected since we effectively increase the capacitance and inductance of the readout resonator. The readout resonator ω_r decreases since it is inversely proportional to the square root

of the capacitance and the inductance of the readout resonator. In the right plot of Fig. 3.11 we can see that the anharmonicity of the qubit, mode 1 in the plot, is relatively insensitive to changes in the readout resonator, as expected. The anharmonicity of the readout resonator is 0 since it is a non-linear element. The same behavior is shown in the right plot of Fig. 3.13.

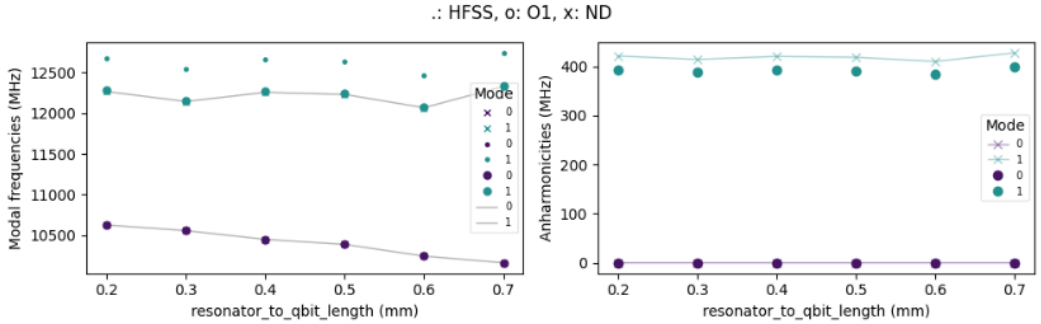

Figure 3.11.: Simulation of the frequency (left plot) and anharmonicity (right plot) of the system for different values of the parameter resonator to qubit length defined in Fig. 3.10. Mode 0 corresponds to the readout resonator element and mode 1 corresponds to the qubit element.

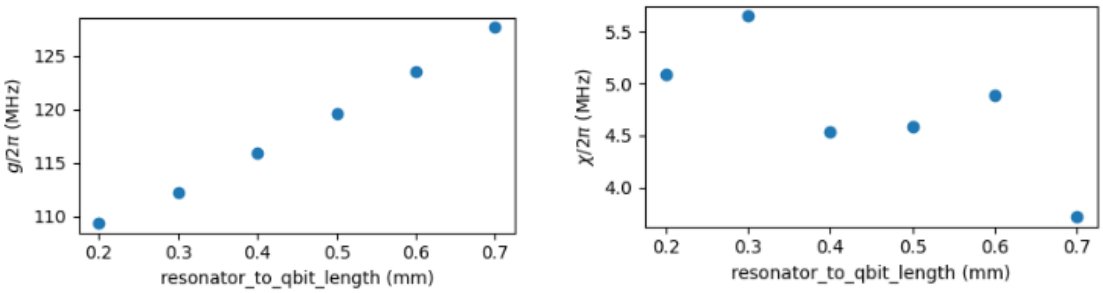

a b

Figure 3.12.: Coupling strength g (subplot **a**) and dispersive shift χ (subplot **b**) between the qubit and the readout resonator for different values of the parameter resonator to qubit length defined in Fig. 3.10.

Furthermore, as expected, the coupling strength can be controlled by increasing the parameter resonator to qubit length as shown in Fig. 3.12a. This is because the resonator gets closer to the left capacitor pad of the qubit and therefore the electric field of the readout resonator is closer to the qubit. As a consequence, the overlap integral between the dipole of the qubit and the electric field of the readout resonator, which is proportional to coupling strength according to Eq. 2.9, increases. In Fig. 3.12b we see that the dispersive shift χ is relatively insensitive to changes in the parameter resonator to qubit length. This can be explained by Eq. 2.11 where the effect of an increased g, is counteracted by the increased detuning $\Delta = w_q - w_r$.

Another relevant parameter to tune the device is the parameter resonator meander length defined in Fig. 3.10. As we increase the resonator meander length of the readout resonator, we see that the frequency of the readout resonator decreases, as shown in Fig. 3.13. This is because the capacitance and the inductance of the readout resonator increase and since the frequency is inversely proportional to the square root of the capacitance and inductance, the frequency will decrease.

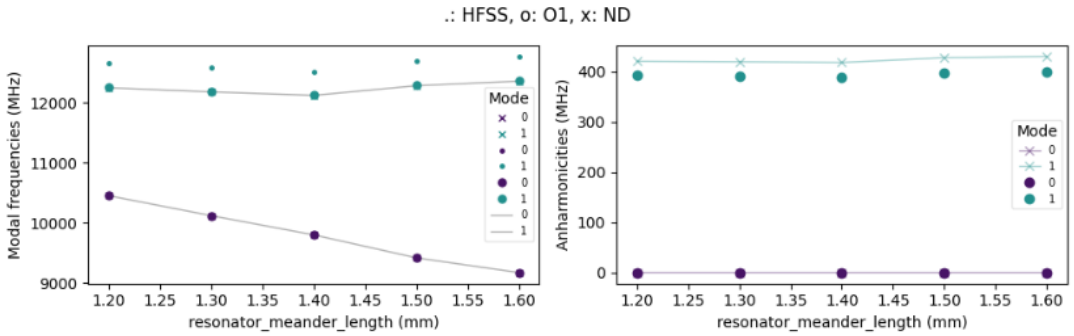

Figure 3.13.: Model frequencies, i.e. qubit and readout resonator frequency (left plot), and anharmonicity (right plot) for different values of the parameter resonator meander length defined in Fig. 3.10.

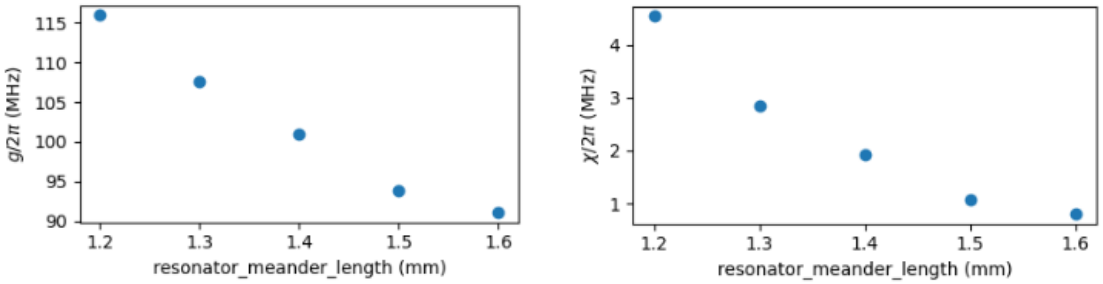

a b

Figure 3.14.: Coupling strength g (subplot **a**) and dispersive shift χ (subplot **b**) between the qubit and the readout resonator for different values of the parameter resonator meander length defined in Fig. 3.10.

Furthermore, the coupling strength g decreases as we increase the meander length of the readout resonator as shown in Fig. 3.14a. This effect is somewhat unwanted since the idea of the redesign was to decouple g from ω_r and control g only via the parameter qubit to resonator length. However, the results shown in Fig. 3.14a can be explained by the substantial decrease in ω_r which has the effect that the field strength of the readout resonator is smaller and therefore, according to Eq. 2.9, g decreases. Furthermore, the dispersive shift decreases as we increase the parameter resonator to meander length as shown in Fig.3.14b. After understanding how the device properties behave with respect to changes in the parameters, we iteratively sweep the parameters until we reach the

targeted properties of the device. Most importantly, for this redesigned device, we were targeting a dispersive shift $\chi/2\pi$ of around 2 MHz, a qubit frequency of around 12.6 GHz and a readout resonator frequency of around 10 GHz. We chose to decrease the dispersive shift compared to the dispersive shift of the measured qubits, which had a large dispersive shift $\chi/2\pi > 5$ MHz as shown in table 4.2 in the next chapter. Note that the dispersive shift needs to be larger than the linewidth of the readout resonator for the dispersive readout to work. However, for the measured samples, the dispersive shift was significantly larger than the linewidth of the readout resonator. This is unnecessary since a large dispersive shift causes larger qubit frequency fluctuations for a given amount of thermal photons in the readout resonator. Therefore the dephasing of the qubit due to thermal noise in the readout resonator increases according to Eq. 4.1 which will be introduced in the next chapter. Furthermore, a large dispersive shift means that the coupling strength between the qubit and readout resonator is large according to Eq. 2.11, which causes a larger Purcell decay, according to Eq. 2.12.

The size of the antenna can be optimized to have optimal electromechanical and optomechanical interaction for the transduction protocol, in the final simulations the antenna diameter was changed to an optimized design. The new optimal antenna diameter was provided by other members of the HYQU group. After iteratively changing the device parameter we reach a set of parameters shown in table 3.1 with which we can roughly reach the targeted device properties shown in table 3.2 according to our simulations. Note that the simulations are performed with the HBAR chip made out of a quartz HBAR, since the presence of the HBAR as well as the material of the HBAR affect the simulations results. This is especially relevant since we are targeting a qubit frequency of $\omega_q/2\pi = 12.65$ GHz that matches the Brillouin frequency of quartz.

Device parameter:	**Value:**
Antenna inner radius	253 μm
Antenna outer radius	200 μm
Resonator meander length	1.05 mm
Resonator conductor width	0.8 mm
Resonator to qubit length	0.9 mm

Table 3.1.: Final device parameters after iteratively sweeping the parameters to reach the targeted device properties

In conclusion, although we could not completely decouple g and ω_r, the redesigned readout resonator offers improved tunability of the coupling strength, and thereby also of the dispersive shift, by introducing an additional resonator lead line to the readout resonator that points towards the left qubit pad. For the future, this design allows for faster fine-tuning of the device parameters. At the time of writing this report, this device has been fabricated but has not been measured yet.

Device property:	**Value:**
Readout resonator frequency $\omega_r/2\pi$	10.05 GHz
Readout resonator frequency $\omega_q/2\pi$	12.62 GHz
Dispersive shift $\chi/2\pi$	2.5 MHz
Coupling strength $g/2\pi$	121 MHz
Transmon regime E_J/E_C	98.6

Table 3.2.: Final device parameters after iteratively sweeping the parameters to reach the targeted device properties

3.4. Simulation of the electromechanical coupling strength of an ħBAR sample

In previous work, coupling between a transmon and an HBAR was performed using a HBAR consisting of a **dome-shaped** AlN film patterned on top of the substrate [28, 29]. In this work, we use an HBAR that consists of a **cylindrical pancake-shaped** AlN film patterned on top of the sapphire substrate, as shown in Fig. 2.3. The properties of the HBAR which is simulated in this section are shown in table 3.3. After fabrication of the HBAR and the high-frequency transmon qubit, the HBAR is flip-chip bonded to the qubit chip. The flip-chip bonding process was previously developed by members of the HYQU group and is explained in the Supplementary material of Ref. [28] as well as in the thesis work performed by Laurant Michaud [31].

Before performing these simulations, the device was measured. The results of the measurement will be discussed in the next chapter in section 4.3. For this discussion, the relevant result from the measurement is that the electromechanical coupling strength was found to be $g/2\pi = 1.38 \pm 0.02$MHz.

Design property:	**Value:**
Pancake radius	200 μm
Pancake height	950 nm
Pillar height	1250 nm
Gap (pillar height - pancake height)	300 nm
Substrate material	Sapphire
Piezo material	AlN
Substrate thickness	420 μm

Table 3.3.: Properties of the AlN on sapphire HBAR which was measured and simulated throughout this work.

We can simulate the coupling rate $g/2\pi$ to different higher-order transverse mechanical modes of the HBAR, specifically, we calculate the coupling rate to the first 10 higher-

order transverse mechanical modes. Note that the modes were simulated using the dimensionality reduced acoustic Schrödingner equation (DASE) simulation method initially developed by Hugo Doeleman and extended by thesis work performed by August Roell [32] at the HYQU group. Here we assume that we have a perfect cylinder, such that the transverse field profile is given by the analytical Bessel functions given in Eq. 2.13. However, DASE does have the ability to simulate an arbitrary HBAR shape and can give insights into losses of the Bessel modes. The process of calculating the coupling strength to the higher-order modes can be described by the following steps:

1. First, the electric field of the qubit mode is exported above the qubit antenna from Ansys, in the center of the AlN piezoelectric material. An image of the exported electric field can be seen in Fig. 3.15. Note that for the exportation the step sizes in the x and y direction are defined, this defines a grid onto which the simulated electric field is interpolated.

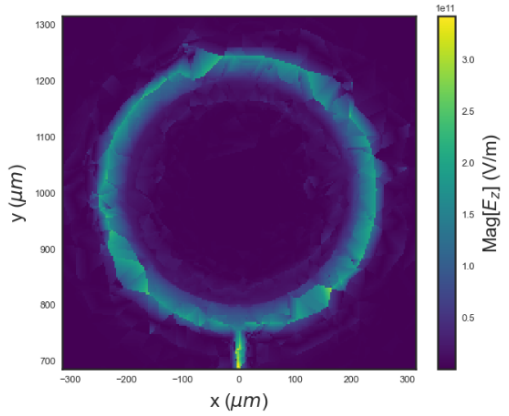

Figure 3.15.: Electric field of the qubit mode above the qubit antenna and in the center depth of the piezoelectric material extracted from Ansys. The mode profiles of the different higher-order transverse mechanical modes are shown in Fig. A.1 of the Appendix section A.1.

2. Next, the mechanical modes of the HBAR are simulated using the DASE simulation package. The mechanical modes are then interpolated onto the same grid as the grid of the electric field. This is crucial for the calculation of the coupling strength. The interpolation was performed using the CloughTocher2DInterpolator provided by the Python package Scipy [33]. The mode profiles of the different higher-order transverse mechanical modes can be seen in Fig. A.1 in the Appendix section A.1.

3. Finally, the coupling strength is calculated according to Eq. 2.21 where $E_z(x, y)$ is the electric field of the qubit, as exported by Ansys HFSS, and $f(x, y)$ is the normalized transverse mode profile of the mechanical modes of the HBAR as simulated by DASE.

4. In case a sweep of a parameter in the design is performed, this process is done for every instance of the sweep such that the coupling strength can be calculated for all variations of the design.

The results of the simulation are shown in Fig. 3.16. From the simulation, we see that we couple to multiple higher-order transverse mechanical modes. From the measurements, we could not discern any of the higher-order transverse modes in our spectroscopy measurements which hints that we couple to an effective mode that consists of many higher-order transverse modes. We can deduce that the coupling rate that was measured is an effective coupling rate to this large collective mode that consists of many higher-order transverse mechanical modes. To support this claim, the frequency spacing between the five higher-order transverse modes with the largest contribution to the coupling rate is simulated to be smaller than 1 MHz, which is smaller than the measured coupling rate of $g/2\pi = 1.38 \pm 0.02$MHz. Note that for the simulations below we choose to calculate an effective coupling rate to 10 higher-order transverse modes. For the reasons stated above we neglect the freqeuncy spacing between the modes and can calculate the effective coupling rate $g_{eff} = \sqrt{\sum_i |g_i|^2}$ where g_i are the individual coupling rates to the higher-order transverse mechanical modes. Using this relation, we can calculate an effective coupling rate of $g_{eff} = 5.8$ MHz. This effective simulated coupling rate is larger than the measured coupling rate of $g/2\pi = 1.38 \pm 0.02$MHz. In the next chapter, we will discuss how the effective coupling rate was calculated from the experimental data. A possible explanation for this discrepancy is that there might be an uncertainty in the properties of the fabricated HBAR shown in table 3.3. To test this hypothesis we can sweep the HBAR properties and simulate the coupling strength for each instance of the simulation to calculate the effective coupling rate.

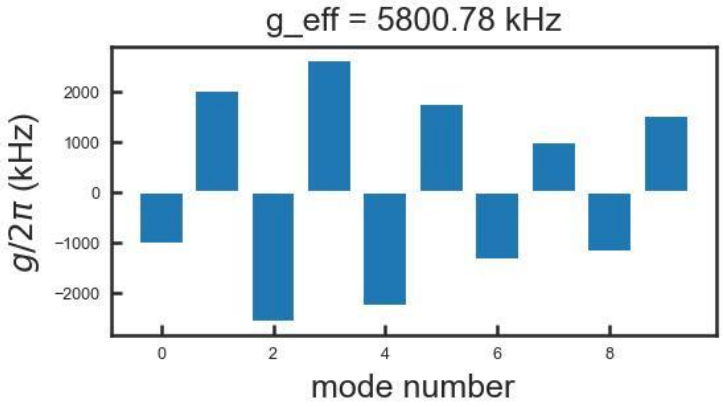

Figure 3.16.: Coupling rate between a high-frequency qubit and different higher-order transverse mechanical modes of an HBAR that consists of pancake-shaped AlN film patterned on top of the sapphire substrate. The mode number describes the beam profile of the higher-order transverse mechanical mode.

Fig. 3.17 shows the calculated coupling strength to all the higher-order transverse mechanical modes as well as the effective coupling strength, while sweeping the chip spacing, which describes the gap between between the qubit antenna and the AlN film on the HBAR chip. From the results, we see that the coupling strength is relatively insensitive to variations in the chip spacing.

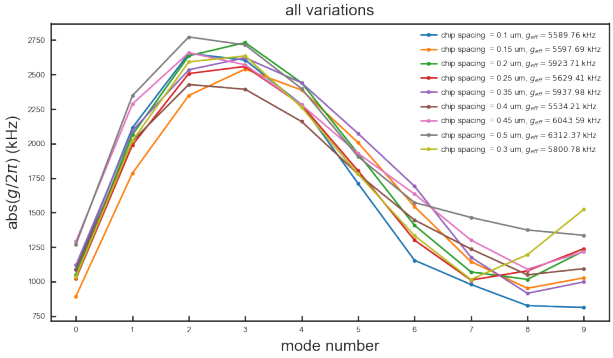

Figure 3.17.: Coupling strength to different higher-order transverse mechanical modes when sweeping the chip spacing.

Fig. 3.18 shows the same simulations as the simulation in Fig. 3.17, but instead we sweep the pancake height. In this simulation, we see a significant change in the coupling strength. For example for a pancake height of 0.9 μm we get an effective coupling rate of $g_{eff} = 1.2$ MHz which is much closer to the measured coupling rate. Furthermore, we can see that as we increase the height of the piezo, the difference in the individual coupling strength between consecutive simulations increases first decreases and then plateaus. This can be explained from the cosine term in the coupling strength equation 2.21.

For the simulation in Fig. 3.18 we used the following values for the constants c^p_{33} = 389e9 Pa from Ref. [34], c^s_{33} = 499e9 Pa from Ref. [35], e^p_{33} = 1.55 C/m^2 taken from Ref. [34] and sound velocity in the AlN piezo v_p = 10.9 km/s from Ref. [34]. When using different constants c^p_{33} = 267e9 Pa [35],v_p = 9.06 km/s from Ref. [35], e^p_{33} = 1.75 C/m^2 (here we use Ref. [36] where the values shown are between 1.5 C/m^2 and 2 C/m^2 and we decide to take 1.75 C/m^2 to be in between the possible range of values) and using the same sapphire stress tensor as before c^s_{33} = 499e9 Pa the values of the coupling strength are significantly larger than the measured coupling rate. This is shown in Fig. 3.19. This complicates the interpretation of the results. One way to determine which set of constants should be used is to measure more samples to get a larger sample set of effective coupling rates and then run the simulation with the different sets of constants to determine when the simulations match the experimental data. Another possible improvement is to measure the thickness of the piezoelectric AlN film more precisely and thereby calculating the speed of sound in the piezo by evaluating the free spectral range (FSR) modulation over a wide frequency range of acoustic modes.

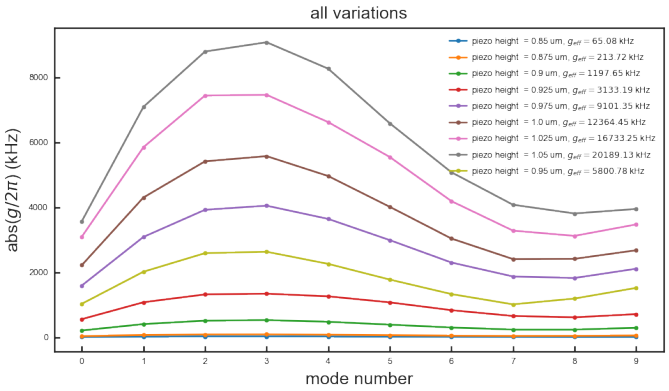

Figure 3.18.: Coupling strength to different higher-order transverse mechanical modes when sweeping the piezo height. The coupling strengths are calculated according to Eq. 2.21 while using the constants c_{33}^{p} = 389e9 Pa from Ref. [34],v_p = 10.9 km/s from Ref. [34], c_{33}^{s} = 499e9 Pa from Ref. [35] and e_{33}^{p} = 1.55 C/m^2 taken from Ref. [34].

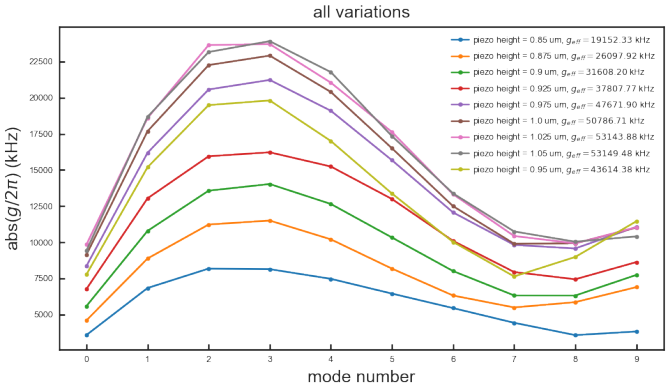

Figure 3.19.: Coupling strength to different higher-order transverse mechanical modes when sweeping the piezo height. The coupling strengths are calculated according to Eq. 2.21 while using the constants c_{33}^{p} = 267e9 Pa [35],v_p = 9.06 km/s from Ref. [35], e_{33}^{p} = 1.75 C/m^2 [36] and c_{33}^{s} = 499e9 Pa [35].

In conclusion, we were able to simulate the coupling strength between the qubit and the HBAR. From the simulation, we can deduce that when using one set of constants, and considering possible uncertainty in the fabrication, we simulate an effective coupling strength that is close to the measured coupling strength. For future predictions of the coupling strength of different samples, fine-tuning of the simulations should be performed to determine more precise values for the constants of the materials that we use in our devices. In the next chapter of this report, we will present the different measurement results obtained throughout this work and discuss the results.

Chapter 4

Experimental results

In this chapter of the report, we will present measurement results attained throughout this work. First, we will briefly explain the measurement setup used to measure the devices, which is based on standard measurement techniques from cQED. Next, We will present the experimental procedure to characterize the high-frequency transmon qubits and present detailed measurement results for one of the qubits measured in this work. Based on the measurement results we can extract relevant properties of the device, for example, the Purcell limit of the device or the coupling strength between the qubit and the readout resonator. Furthermore, we will present a summary of all the three high-frequency qubits measured and discuss the results. Additionally, we will discuss possible explanations for the low lifetimes of the qubits.

Lastly, we will present the results of a sample consisting of a high-frequency qubit flip-chip bonded to an HBAR made of an AlN film patterned on top of a sapphire substrate. Although this device will not be used as the final device for the transduction experiment, which is currently envisioned to be performed using an HBAR consisting of a quartz substrate as explained in previous chapters, this measurement is the first measurement performed using a high-frequency qubit bonded to an HBAR. We will investigate whether we can electromechanical couple to an HBAR with the high-frequency qubit and characterize the device. We will present selected measurements that are crucial to understanding the device and discuss key results as well as some difficulties encountered throughout the measurement.

Note that the high-frequency qubits were fabricated by Rodrigo Benevides. Additionally, the HBAR used in this work was fabricated by Max Drimmer and the flip-chip bonding of the qubit chip to the HBAR was done by Rodrigo Benevides.

4.1. Experimental setup

The measurements performed throughout this work were done using standard techniques from cQED, we refer to Ref. [37] for an introduction to experimental quantum measure-

ment of superconducting qubits. The readout of the state of the qubit is performed via the dispersive coupling between the qubit and the on-chip readout resonator. To control and readout the state of the qubit we use microwave pulses using in-phase and quadrature mixers (IQ-mixers). The control of the microwave pulses and the acquisition of data is performed by a Quantum Machines OPX device, which is a field programmable gate arrays (FPGA)-based arbitrary wave generator (AWG). Since our devices operate at higher frequencies than typical cQED experiments, we use IQ-mixers, filters and circulators that are compatible at the higher frequencies of the devices.

The samples are placed inside a dilution refrigerator and attached to its base plate which is cooled down to temperatures of around 10 mK. This temperature is required to ensure that the energy of thermal photons, which is given by $k_B T$, where k_B is the Boltzmann constant and T is the temperature, is much smaller than the energy $\hbar\omega_{ge}$ required to excite the qubit from the ground to the excited state, i.e. the g-e transition. Another reason why we need low temperatures is that our qubits are fabricated using aluminum as the superconducting material, and since the critical temperature for aluminum is $T_c = 1.2$ K [37], we have to be below this temperature to have a superconducting qubit.

4.2. Measurements of high-frequency qubits

Throughout this work, we measured 3 high-frequency qubits. The characterization of the qubits can be performed within a few days, depending on various experimental difficulties. For example, the first samples of a fabrication run are typically more time-consuming since the resonance frequencies of the readout resonator and the qubit can only be predicted from simulations and all pulses need to be calibrated from scratch. Measurement of subsequent devices is typically faster since the device parameters can be approximated from previous measurements.

Note that the measurements are performed via the dispersive coupling between the on-chip readout resonator and the qubit. All measurements that were taken in this work are done in transmission via the input and output pins of the tunnel cavity, as shown in Fig. 3.4. The readout resonator is driven via the input pin and the transmitted field of the readout resonator is measured via the output pin and contains the necessary information to determine the state of the qubit [37].

4.2.1. Measurement procedure

In this subsection, we will present the standard measurement procedure to characterize the devices measured throughout this work:

1. First, we calibrate the IQ-mixers used to generate and modify the required microwave pulses for the measurements. This is done by an automatized software that modifies the amplitude and phase of the quadrature signals such that the IQ-mixers suppress the LO leakage and reject the image of the signal generated by the IQ-mixers. For more information on IQ-mixers, we refer to [38]. Note that the calibration depends on the frequency, pulse amplitude and length of the microwave pulses that are used for the calibration. If drastic changes to any of these parameters are made throughout the measurement, the calibration has to be redone.

2. Next, we perform a spectroscopy measurement on the readout resonator, to determine its resonance frequency ω_r. An example of this measurement is shown in Fig. 4.1a. Furthermore, to measure the bare linewidth of the readout resonator κ_r we reduce the amplitude of the pulse used for the spectroscopy until the linewidth is approximately unchanged. The use of a low pulse amplitude ensures that we see the resonance with its bare linewidth by avoiding power-broadening.

3. After determining the readout resonator frequency, we can measure the qubit frequency ω_q. This is performed via a pulsed two-tone spectroscopy sequence. The first pulse has a frequency that is swept to find the qubit frequency. The second pulse is played at the readout resonator frequency ω_r and probes the readout resonator on resonance. When the frequency of the first pulse is resonant with the qubit frequency ω_q, the qubit is excited and therefore the readout resonator frequency is shifted due to the dispersive coupling. This causes the transmitted signal to drop as shown in Fig. 4.1b.

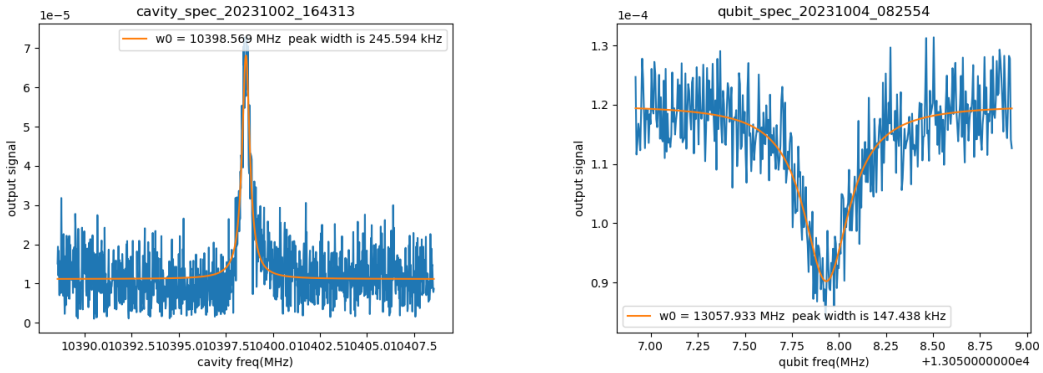

a b

Figure 4.1.: **a:** Spectroscopy of the readout resonator. From the measurement, we find the resonance frequency ω_r as well as the linewidth κ_r of the readout resonator. **b:** Spectroscopy of the qubit to determine the resonance frequency ω_q of the transition between the ground and excited state of the qubit.

4. After determining the resonance frequencies we want to measure the properties and quality of the qubit. For this, it is necessary to find the π-pulse amplitude at a given pulse length. The π-pulse excites the qubit from the ground to the excited state. To determine the π-pulse amplitude we perform a Rabi amplitude measurement that consists of sweeping the amplitude of the pulse used to drive the qubit. Since the qubit is an effective two-level system we will observe Rabi oscillations between the ground and the excited state. By fitting the trace of the output signal, we can determine the amplitude necessary to perform a π-pulse on the qubit, as shown in Fig. 4.2a. Note that by observing Rabi oscillations, we confirm that the system is a qubit.

5. To determine the lifetime of the qubit, also known as the T_1 time, we first perform a π-pulse on the qubit to prepare it in the excited state. Then, we wait a variable time t and then measure the qubit state via the readout resonator. By fitting the data with an exponential function we can determine the T_1 time as shown in Fig. 4.2b.

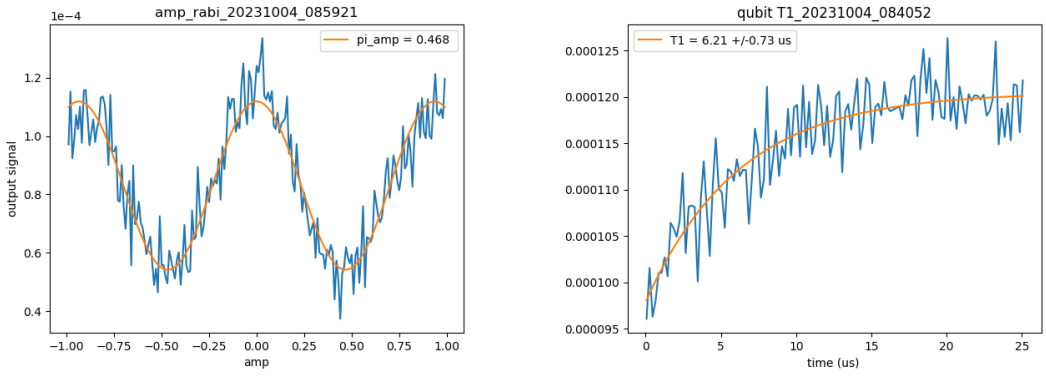

a b

Figure 4.2.: **a:** Rabi amplitude measurement to determine the correct amplitude of a π-pulse for a pulse length of 2 μs. Subsequent measurements were performed using a shorter pulse length of 1 μs and the pulse amplitude was adjusted inversely. **b:** Measurement of the lifetime (T_1) of the qubit.

6. To characterize the dephasing time, known as the T_2 time, we perform a Ramsey-type measurement. First, we apply $\pi/2$-pulse on the qubit to prepare it in an equal superposition of the g and e-state. Then we wait for a variable time t, perform another $\pi/2$-pulse and measure the qubit state via the readout resonator. The result of the measurement is shown in Fig. 4.3a, where from the fit of the data, which is done by a function consisting of an exponential times a sine function, we can extract the T_2 dephasing time which is the decay time of the exponential. Note that the signal is oscillating, even though we measure in the rotating frame because for the measurement the pulses are played slightly detuned from the qubit

frequency. This detuning is shown in the legend of the plots in Fig. 4.3. By setting a certain detuning, Δ, and fitting the oscillations, we can compare the result of the fit to the value of Δ that we set. If there is a large difference, the qubit frequency is not well calibrated. Therefore, this measurement can be used to fine-tune the qubit frequency.

7. The T_2 echo measurement is similar to the T_2 measurement but with an additional π-pulse between the two $\pi/2$-pulses. This has the effect that the T_2 echo is less sensitive to low-frequency noise. The result of the measurement is shown in Fig. 4.3b, where the same fit of the data is performed as for the T_2 measurement. Typically the T_2 echo time is larger than the T_2 time.

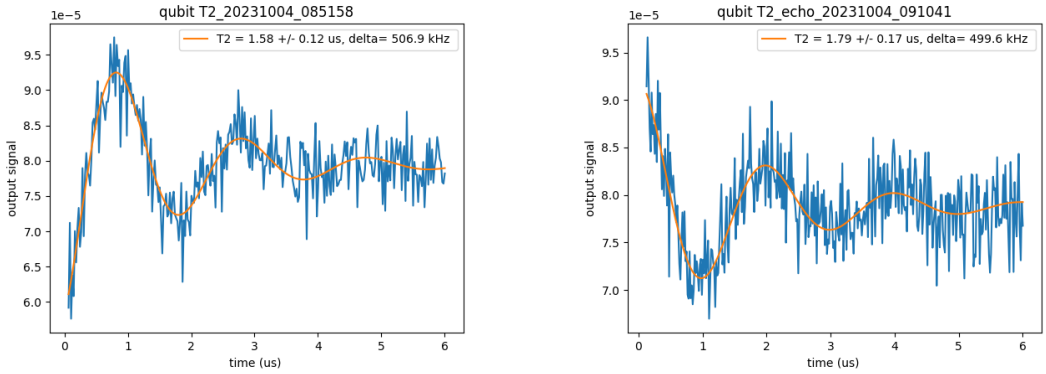

a b

Figure 4.3.: **a:** Measurement of the dephasing time (T_2). **b:** Measurement of the T_2 echo dephasing time of the qubit. Compared to the standard T_2 measurement the T_2 echo measurement pulse sequence eliminates low-frequency noise acting on the qubit.

8. To determine the dispersive shift χ of the system, we perform a measurement that consists of readout resonator spectroscopy, but before the spectroscopy is performed, a π-pulse is played to excite the qubit. Due to the dispersive coupling between the readout resonator and the qubit, we will see a peak shifted by χ from the bare readout resonator frequency. This is shown in Fig. 4.4. Note that we also see a peak at the bare readout resonator frequency. This is because the lifetime of the qubit is relatively short, and since the measurement data is an average of many measurements, in some of the measurement sequences, the qubit relaxes back to the ground state before the spectroscopy is finished. For these measurements, a peak will be observed in the bare readout resonator frequency since the qubit is not in its excited state and therefore does not shift the readout resonator frequency.

9. To determine the e-f transition frequency between the first excited state and the second excited state of the qubit, we perform a measurement called e-f spectroscopy.

The measurement consists of exciting the qubit to the first excited state using a π-pulse and then sending a probe tone at varying frequencies, similar to point 3. This allows us to measure the e-f transition since when the probe tone is on resonance with the e-f transition, some of the population in the e-state is transferred to the f-state. After that, a final π-pulse on the g-e transition is performed. Depending on the probe tone frequency, not all the population will be recovered to the g-state and we will see a dip in the spectrum when the probe tone is resonant with the e-f transition. The e-f transition frequency is shifted by the anharmonicity α of the qubit from the g-e transition frequency ω_q. An example of the e-f spectroscopy is shown in Fig. 4.5a.

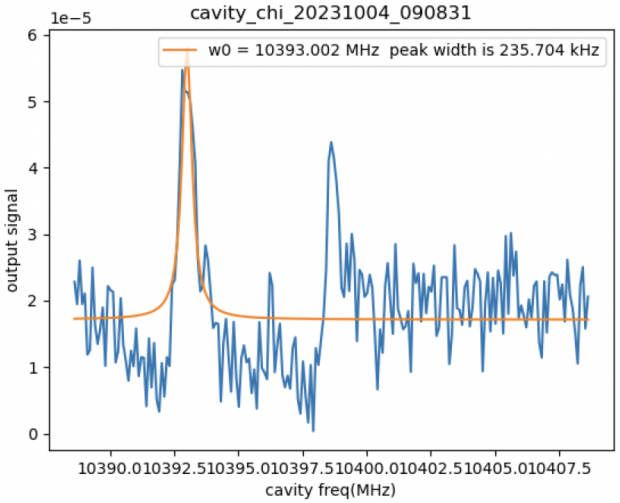

Figure 4.4.: Measurement to determine the dispersive shift χ. The measurement consists of a g-e π-pulse on the qubit followed by a cavity spectroscopy. Due to the dispersive coupling between the qubit and the readout resonator there is a second peak in the spectroscopy trace. The frequency difference between the two peaks is χ.

10. To determine the pulse amplitude for a given pulse length to excite the qubit from the first excited to the second excited state we perform a Rabi amplitude measurement on the e-f transition. An example of this measurement is shown in Fig. 4.5b.

11. To determine the thermal population of the qubit we perform two measurements: The first measurement is equivalent to an e-f Rabi amplitude measurement from which we can get the amplitude A, which is the amplitude of the oscillations we see in the Rabi trace. The second measurement is similar to an e-f Rabi amplitude but without performing a π-pulse on the g-e transition. We measure the amplitude A_0 of the Rabi oscillations of the ef-transition without the first π-pulse on the

g-e transition that populates the excited state. If the qubit was perfectly in the ground state, we would see no oscillations. However, since there is some population of the qubit in the excited state due to it having a finite temperature, there is an oscillation with a small measurable amplitude. These measurements are shown in Fig. 4.6. By comparing the amplitudes of the two measurements we can obtain the qubit e-state thermal population n_e given by $n_e = \frac{A_0}{A+A_0}$. In the regime where most of the population is in the g-state, the population n_e is approximately equal to the average number of excitations $n_{thermal}$. From the qubit population, we can calculate the effective temperature according to the Bose-Einstein distribution.

$$n_{thermal} = \frac{1}{\exp \frac{\hbar\omega_q}{k_B T} - 1} \tag{4.1}$$

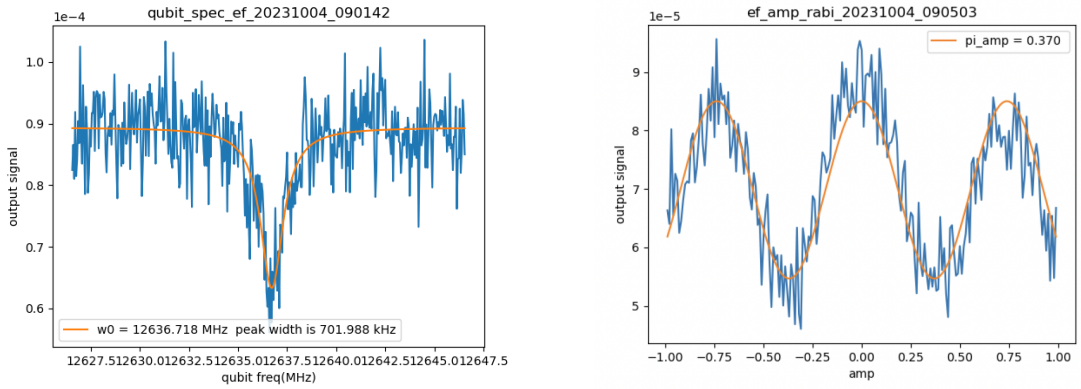

a b

Figure 4.5.: **a:** Spectroscopy of the qubit to determine the resonance frequency of the transition between the first excited state and the second excited state. **b:** Rabi amplitude measurement to determine the correct amplitude of a π-pulse to excite the qubit from the first excited state to the second excited state.

4.2.2. Comparing measurements to simulations

As explained in the previous chapter, we can perform simulations of the devices using Ansys and the pyEPR package. In this section, we will compare the measurements of both the simulation method based on numerical diagonalization **ND** and the method based on first-order perturbation theory **O1**. In table 4.1 we show a comparison of the first measured qubit and the results of the two simulation methods. Note that for the simulations of the device, we use the Josephson inductance $L_J = 3.43$ nH, which was inferred from a junction resistance measurement at room temperature measurement.

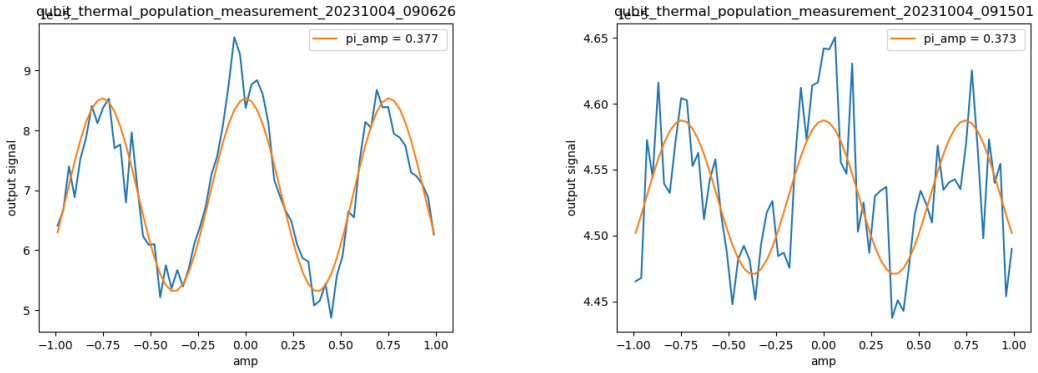

a b

Figure 4.6.: To determine the thermal population of the qubit we perform two measurements: Measurement to determine the Rabi amplitude A of the e-f transition with (**a**) and without (**b**) performing a π-pulse on the g-e transition before measuring the Rabi oscillations of the e-f transition.

In the table, we see that the qubit frequency is simulated to be significantly higher with both simulation methods than it is in the measured device. A possible explanation for this is that the value of L_J which was used to simulate the device is smaller than the L_J of the device when it was cooled down. The value of L_J used for the simulations was inferred from a junction resistance measurement at room temperature using the Ambegaokar-Baratoff formula [39] and a calibration factor that scales the measured room temperature resistance to the expected resistance at low temperature. This calibration factor is probably miscalibrated and thereby the L_J deviates from the value of L_J when the device is cooled down, as shown in the table. Since the qubit frequency scales with $\sqrt{1/L_J}$ according to equation 2.6, this partially explains why we measure a lower frequency. Other simulations are closer to the measured properties, except for χ which is only predicted well by the **ND** simulation method and g which is only predicted well by the **O1** simulation method.

Note that in table 4.1,we presented some relevant device properties of the qubit and the readout resonator that were calculated using the measured data. Next, we will present how these quantities are calculated from the measured data: the anharmonicity α can be deduced by comparing the frequencies between the g-e transition shown in Fig. 4.1b and the e-f transition as shown in Fig. 4.5a. By subtracting the two transition frequencies we attain α. From the anharmonicity, we can deduce the charging energy E_C via the Eq. 2.7, which states that $E_C \approx -\hbar\alpha$. Note that this approximation holds as long as we are in the transmon regime. Furthermore, the coupling strength g can be calculated by solving Eq. 2.11 for g since both the detuning $\Delta = \omega_q - \omega_r$ and the dispersive shift χ are given from our measurements. Using Eq. 2.6 we can calculate the Josephson energy E_J since we know the frequency of the qubit ω_q as well as the charging energy E_C as

Quantity	MMT CD21 (TR1)	Simulation O1	Simulation ND
$g/2\pi$	199.2 MHz	204.0 MHz	248.6 MHz
$\alpha/2\pi$	−421 MHz	−421 MHz	−433 MHz
$\chi/2\pi$	−5.6 MHz	−3.4 MHz	−5.6 MHz
Ej/Ec	128	100	93
L_J	3.03 nH (3.43 nH *)	3.43 nH	3.43 nH
Qubit freq $\omega_q/2\pi$	13.0 GHz	14.3 GHz	14.3 GHz
RR freq $\omega_r/2\pi$	10.4 GHz	10.6 GHz	10.6 GHz

Table 4.1.: Comparison of the measured device properties of the first qubit measured in this work to simulations performed with the O1 method and the ND method. *: This value of L_J was inferred from a junction resistance measurement at room temperature.

explained above. Since we now know both E_C and E_J we can calculate the ratio E_J/E_C to determine whether we are in the transmon regime. Additionally, we can calculate the Josephson inductance L_J using Eq. 2.2. Lastly, the Purcell-limited lifetime $T_{purcell}$ can be computed according to Eq. 2.12 to determine whether our qubit is Purcell-limited. The Purcell-limited lifetime for the measured qubits will be calculated and will be shown in table 4.2 in the next subsection.

4.2.3. Comparison of 3 high-frequency qubits

In this subsection, we will present the measurement data and calculated properties of three high-frequency qubits measured in this work. The results of the first qubit, named TR1, which was measured in cooldown 21 (CD21), have already been discussed in detail above. The other two qubits, TR2 and TR3, which were measured in CD22 and CD23 respectively were characterized following the standard measurement procedure above. All the results of the three qubits are shown in table 4.2. The first two qubits measured are nominally the same and only had a small difference in the L_J which was inferred from a junction resistance measurement at room temperature. Note that in the fabrication process, we expect a spread in the L_J. The last qubit (TR3) was fabricated with slightly rounded corners compared to the first two qubits.

The desired frequency range that we are targeting is around 14 GHz for the bare qubits. This is because when we flip-chip bond the qubit to the HBAR the frequency decreases such that we will be close to the targeted frequency of 12.65 GHz. From the table 4.2, we see that the qubits are slightly lower than the desired frequency. As mentioned above, the last qubit (TR3) was fabricated with slightly rounded corners compared to the first two qubits. The idea of this is that sharp edges in the device are typically regions where higher losses occur, which could lead to worse lifetimes of the qubit. This was not the

case and in fact, this qubit had lower T_1 and T_2 times.

Quantity	**CD21 (TR1)**	**CD22 (TR2)**	**CD23 (TR3)**
$g/2\pi$	199.2 MHz	201.7 MHz	205.8 MHz
$\alpha/2\pi$	-421 MHz	-421 MHz	-433 MHz
$\chi/2\pi$	-5.6 MHz	-5.7 MHz	-9.4 MHz
E_J/E_C	128	128	114
L_J	3.03 nH (3.43 nH *)	3.02 nH (3.30 nH *)	3.31 nH (3.43 nH *)
$T_{purcell}$	115.3 μs	88.6 μs	25.9 μs
Qubit freq $\omega_q/2\pi$	13.05 GHz	13.08 GHz	12.66 GHz
RR freq $\omega_r/2\pi$	10.31 GHz	10.41 GHz	10.45 GHz
$\kappa_{rr}/2\pi$	245.0 kHz	316.2 kHz	705.1 kHz
T_1	6.2 ± 0.7 μs	6.5 ± 0.7 μs	5.2 ± 0.3 μs
T_2	1.6 ± 0.1 μs	1.8 ± 0.2 μs	0.7 ± 0.1 μs
T_2 echo	1.8 ± 0.2 μs	1.9 ± 0.4 μs	Not measured
E-state population	3.5%	5.6%	8.5%
Effective temperature	185 mK	215 mK	239 mK

Table 4.2.: Properties of the three measured high-frequency qubits.
*: This value of L_J was inferred from a junction resistance measurement at room temperature.

The relation between T_1, T_2 and T_ϕ is given by $\frac{1}{T_2} = \frac{1}{2T_1} + \frac{1}{T_\phi}$ from which we can deduce that $T_2 \leq 2T_1$ where equality is provided when $T_\phi \to \infty$. The T_2 of the qubit is said to be T_1 limited if $T_2 = 2T_1$ which is not the case for our qubit as can be understood from table 4.2. Furthermore, the measured lifetimes of all qubits are much smaller than the Purcell-limited lifetime $T_{purcell}$. Note that we decreased the Purcell limited lifetime of the last qubit intentionally, by increasing the output coupling, such that we have an improved readout.

From the measurements we see that the lifetimes of the qubits are low compared to other transmon qubits at the typical frequencies of 4-8 GHz, which were fabricated in recent years with a similar fabrication process in the HYQU group, where lifetimes in the order of $T_1 = 30$ μs are measured for qubits which are not bonded to an HBAR [28]. Assuming a similar quality factor Q in the fabrication of our high-frequency qubits to standard transmon qubits we expect a lower T_1 lifetime due to the relation $Q = 2\pi \cdot f \cdot T_1$. This itself still does not fully explain the low T_1 of our system. Some hypotheses for the lower T_1 and T_2 of our system are:

1. We observed higher effective temperatures than the usual temperatures which are well below 100 mK. This can lead to lower T_2 times since the resonator population leads to dephasing of the qubit via the dispersive interaction. In section 4.3.3 we

perform measurements to check whether this higher effective temperature limits our T_2 times. This analysis was only performed for the hybrid device consisting of a qubit flip-chip bonded to an HBAR which will be discussed in the next section. A possible explanation for the high temperatures is that the high-frequency filter at the input line does not suppress noise well enough at the higher frequencies of the device. Another plausible explanation for the higher effective temperatures could be that the filters introduce additional thermal noise in the fridge due to bad thermalization of the filter to the base plate of the dilution refrigerator.

2. Another hypothesis, which could explain the low lifetimes of our qubits, is that our qubit design has a higher energy participation ratio in lossy regions, for example, the interfaces between materials such as metal and substrate. This is currently being investigated by other members of the HYQU group, namely Tom Schatteburg, and depending on the analysis future modifications of the qubit geometry could be made to improve the quality of the qubit.

3. So far, only two fabrication runs of the qubits have been performed. It is therefore possible that by fabricating and measuring more qubits we could have better statistics and possibly higher T_1 and T_2 times.

4.3. Measurements of a $\hbar$BAR device

In this section, we will discuss the measurement of the HBAR, consisting of a pancake-shaped AlN piezoelectric film patterned on top of a sapphire substrate, which is flip-chip bonded to a high-frequency superconducting qubit on a separate chip. This combined device will be called an $\hbar$BAR in accordance with previous work in the HYQU group. Note that in the context of the quantum transduction project, this device will not be the final device, since the envisioned $\hbar$BAR for quantum transduction will include an HBAR consisting of a quartz substrate instead of sapphire, since quartz has a sufficient optomechanical coupling at lower Brillouin frequency than sapphire, namely at a Brillouin frequency of 12.65 GHz [4], which is the reason why we target this frequency in our qubit design.

The purpose of the measurements of this $\hbar$BAR is to understand whether we can show electromechanical coupling using a high-frequency qubit with a larger qubit antenna compared to previous work [28] as well as study to which higher-order transverse mechanical modes we couple to, as already discussed in subsection 3.4 in the previous chapter.

4.3.1. Measurement of the qubit when flip-chip bonded to an HBAR

Before performing measurements that involve the phonon modes of the HBAR, we measure the properties of the qubit following the same measurements described in the subsection 4.2.1. The results of the measurement are shown in the right column of table 4.3. In the table, we compare the properties of the same high-frequency transmon (TR1) when it was not bonded to an HBAR and when it was bonded to an HBAR.

As expected, the frequency of both the readout resonator and the qubit decreases when the qubit is bonded to an HBAR. This is because the vicinity of the HBAR, being a dielectric, increases the capacitance of the qubit and readout resonator, thereby decreasing its frequency. Additionally, the lifetimes of the qubit decrease, which can be explained by the vicinity of the HBAR which can introduce additional loss channels to the qubit. Examples of loss channels are: high dielectric losses in the piezo, undesired phonon radiation via the piezo or potentially lossy interface between air and the surface of the HBAR. Note that the gap size of 300 nm between the qubit chip and the pancake-shaped AlN film is small compared to other devices. This gap size was chosen to ensure that the coupling strength between the qubit and the phonon modes of the HBAR is sufficiently large. The effect of this is that the lifetimes of the qubit are further reduced.

Furthermore, for the measurement of the $\hbar$BAR, we increased the pin length of the output pin, shown in Fig. 3.4 because we targeted a higher output coupling ratio to be able to perform readout with very short pulses, which is necessary to characterize the device due to its very low lifetimes. The effect of the longer output pin length explains why the Purcell limited lifetime of the qubit decreased as shown in table 4.3.

4.3.2. Characterization of the device

In this subsection, we will present the most important measurements performed to characterize the $\hbar$BAR. The first goal when measuring an $\hbar$BAR is to determine whether we can characterize the phonon modes of the HBAR using the qubit. This can be done in multiple ways. The simplest one is to perform a qubit spectroscopy and see whether there are additional peaks in the spectroscopy. This is shown in Fig. 4.7 where we can see the narrow phonon dips separated by 13 MHz which is the FSR of the HBAR.

To interact with the phonon modes of the HBAR we need to shift the frequency of the qubit to be resonant with the frequency of the phonon modes. This is achieved by using a stark shift drive on the qubit. In Fig. 4.8 we show a measurement of a qubit spectroscopy as a function of the stark shift amplitude. The measurement consists of one qubit spectrum for every stark shift amplitude applied on the qubit. When the qubit is resonant with a phonon mode, we see an anticrossing, also known as an avoided crossing,

where the mode of the qubit and the phonon hybridize. This is present at stark shift amplitudes of approximately 0.06, 0.12, 0.16 and 0.19 in Fig. 4.8 and proves that we can couple the qubit to the phonon modes of the HBAR.

Quantity	**Bare TR1**	**TR1 bonded to HBAR**
$g/2\pi$	199.2 MHz	180.0 MHz
$\alpha/2\pi$	-421 MHz	-275 MHz
$\chi/2\pi$	-5.6 MHz	-6.5 MHz
E_J/E_C	128	209
L_J	3.03 nH (3.43 nH at RT)	2.8 nH
$T_{purcell}$	115 μs	17 μs
Qubit freq $\omega_q/2\pi$	13.05 GHz	11.03 GHz
RR freq $\omega_r/2\pi$	10.4 GHz	9.2 GHz
$\kappa_{rr}/2\pi$	245.954 kHz	959 kHz
T_1	6.2 ± 0.7 μs	0.8 ± 0.02 μs
T_2	1.6 ± 0.1 μs	0.4 ± 0.02 μs
T_2echo	1.8 ± 0.2 μs	1.4 ± 0.1 μs
E-state population	3.5%	NA
Effective temperature	185 mK	NA

Table 4.3.: Comparison of the properties of the bare TR1 qubit to the properties of the same qubit when it is flip-chip bonded to an HBAR.

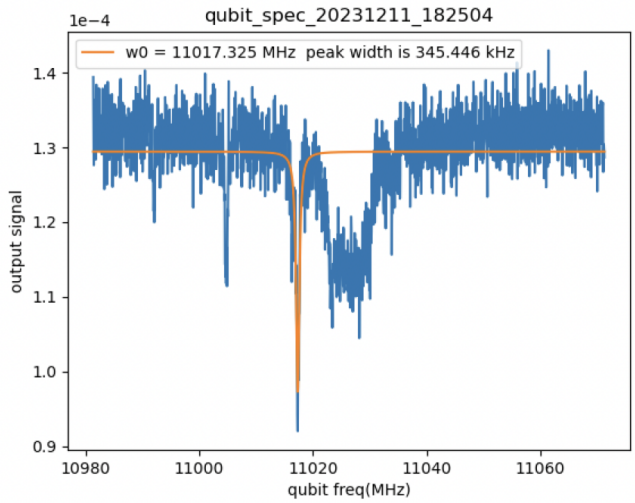

Figure 4.7.: Qubit spectroscopy of the $\hbar$BAR device. The broad dip is the qubit mode. The additional dips are the phonon modes of the HBAR, which are separated by 13 MHz which FSR of the HBAR.

Now that we know that the qubit couples to the phonon modes, we can attempt to coherently exchange energy between the qubit and the phonon. This measurement, which we call phonon 2D Rabi, consists of exciting the qubit to its excited state, then stark shifting it with a variable stark shift amplitude. If the qubit is shifted to a frequency where it is resonant with a phonon mode, the qubit and the phonon mode will exchange excitations, and we observe Rabi-like oscillations between the qubit and the phonon mode. This is shown in Fig. 4.9a, where the chevron pattern, which is typical to this type of measurement, is clearly visible, especially when the qubit is stark shifted with an amplitude of approximately 0.118.

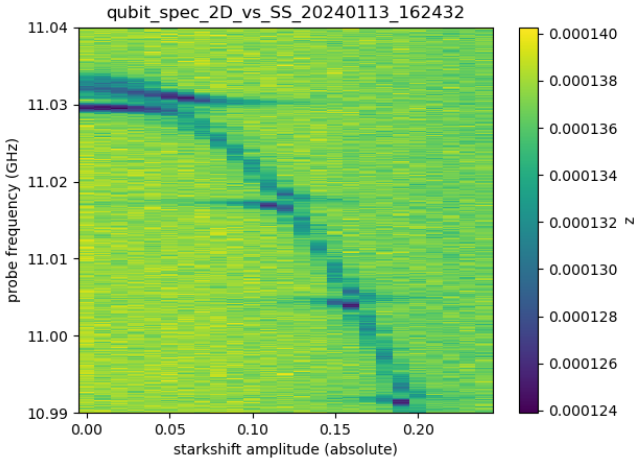

Figure 4.8.: Qubit spectroscopy of the qubit at different stark shift amplitudes applied to the qubit. When the qubit is resonant with a phonon mode of the HBAR an anticrossing is observed.

A crosscut of the phonon Rabi measurement for a stark shift of 0.118 is shown in 4.9b. By fitting the Rabi oscillations one can extract a swap time $\tau = 104$ ns, which is the time it takes the excitation to swap between the qubit and the phonon mode. Additionally an electromechanical coupling strength of 1.38 ± 0.02 MHz can be deduced by fitting the data.

The coupling strength of 1.38 ± 0.02 MHz is large and as discussed in the previous chapter in subsection 3.4 this coupling strength is an effective coupling strength to a collection of higher-order transverse mechanical modes. This is because in the qubit spectroscopy spectrum shown in 4.7 we do not see any other phonon modes, except the phonon modes which are equally spaced by an FSR of 13 GHz of the longitudinal modes. Furthermore, according to our simulations, the total frequency spacing between the five transverse modes with the largest contribution to the coupling strength is smaller than 1 MHz. Since the coupling strength is larger than this frequency spacing, it is a clear indication that we couple to a collection of higher-order transverse mechanical modes.

Lastly, we can measure the T_1 and T_2 times of the phonon modes. The pulse sequence to measure the phonon T_1 starts with exciting the qubit using a π-pulse and stark shifting it to be resonant with the phonon mode that we want to measure. The qubit is kept on resonance for the duration of the swap time τ to exchange the excitation to the phonon mode until it is stark shifted back to its rest point, which could be at 0 stark shift amplitude or at another stark shift amplitude. The excitation is now in the phonon mode and we can wait for a variable time t until we measure the state of the phonon mode by stark shifting the qubit to be resonant with the phonon mode for a time τ to swap back the excitation to the qubit and measure the qubit state via the readout resonator. To measure the T_2 time of the phonon mode we follow the same procedure, with the exception that we start with a $\pi/2$-pulse on the qubit and at the end the pulse sequence with another $\pi/2$-pulse after swapping the excitation back from the phonon mode. For rest point stark shift of 0 amplitude, we measure $T_1 = 1.4 \pm 0.1$ μs and $T_2 = 3.8 \pm 0.3$ μs for mode0 which sits at a frequency $\omega_{mode0} = 11.017$ GHz. This type of measurement with a bulk acoustic resonator was first demonstrated in Ref. [18]. In the next subsection 4.3.3 we will perform calculations to check how much of the dephasing is due to thermal noise in the readout resonator.

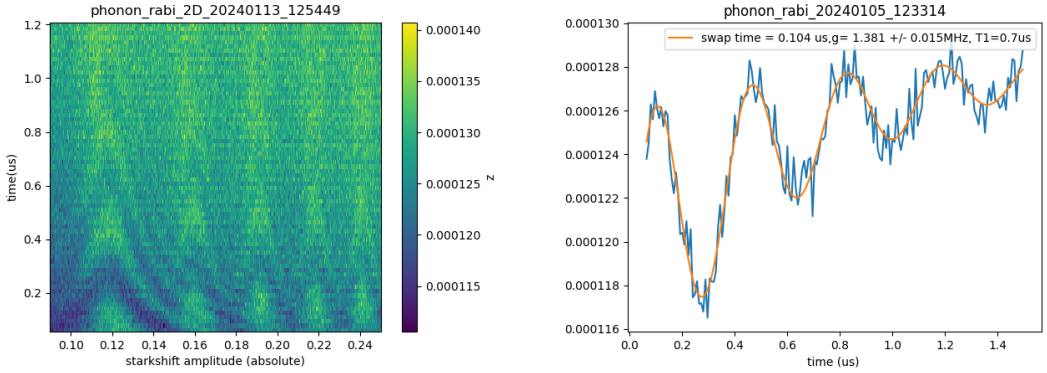

a b

Figure 4.9.: **a:** Phonon 2D Rabi measurement. **b:** Phonon Rabi 1D measurement.

4.3.3. Measuring the thermal population of the readout resonator

To measure the thermal population of the readout resonator, we perform a highly averaged and resolved qubit spectroscopy as shown in Fig. 4.10. Since the readout resonator has a certain amount of thermal noise photons $\bar{n}_{noise}$, we expect an additional dip shifted by χ from the qubit resonance frequency due to the dispersive coupling between the qubit and the readout resonator. Since we measured the dispersive shift χ, we can focus on the area where we expect a dip and calculate the maximally possible dip depth A_{max}. The frequency area we use to estimate A_{max} is between 11.017 GHz and 11.022 GHz.

A_{max} is calculated by subtracting the minimal signal in the area we expect a dip from the maximal signal in that area. We can put an upper bound on $\bar{n}_{\text{noise}} = \frac{A_{max}}{A_{max}+A_{signal}}$, where A_{signal} is the dip depth of the main signal as shown in Fig. 4.10. Using the upper bound $\bar{n}_{\text{noise}} = 0.087$ we can calculate the photon noise-induced dephasing rate using the following equation [40]

$$\Gamma_{\phi}^{\text{noise}} = \frac{\kappa_r \chi^2}{\kappa_r^2 + \chi^2} \bar{n}_{\text{noise}} \,. \tag{4.2}$$

Using this equation the dephasing time due to thermal noise in the readout resonator can be computed: $\Gamma_{\phi}^{\text{noise}} = 0.49$ MHz. Using the measured T_1 and T_2 times and the relation $\Gamma_{\phi} = \Gamma_1 - \frac{\Gamma_2}{2}$ between the loss rates Γ_1, Γ_2 and the pure dephasing rate Γ_{ϕ} we can compute the pure dephasing rate $\Gamma_{\phi} = 1.65$MHz. In this analysis we have put an upper bound on the dephasing due to thermal noise in the readout resonator $\Gamma_{\phi}^{\text{noise}}$ and we can deduce that this is not the only contribution to the pure dephasing since Γ_{ϕ} is significantly larger than the calculated $\Gamma_{\phi}^{\text{noise}}$.

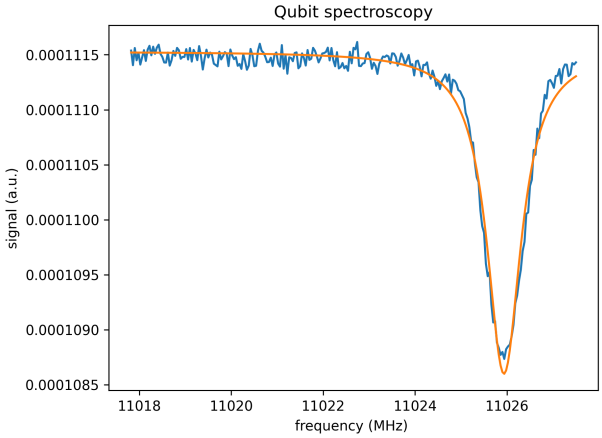

Figure 4.10.: Highly averaged qubit spectroscopy measurement to determine the readout resonator's thermal population. The frequency region we use to estimate the maximum possible dip depth is between 11.017 GHz and 11.022 GHz

4.3.4. Studying the dependence of T_1 on the rest point offset of the qubit

The lifetime of the qubit and the phonon modes depends on the rest point offset applied to the qubit. Qualitatively, we expect that the T_1 of the qubit or the phonon mode will be different when the qubit is stark shifted to be far away from a phonon mode to when the qubit is stark shifted close to a phonon mode. To investigate this behavior, we perform a series of measurements in the following order:

1. First, we calculate a mapping between the stark shift applied to the qubit to the corresponding frequency of the qubit when that stark shift is applied. This is done by fitting the curve of the stark shift vs qubit frequency measurement shown in Fig. 4.8, while neglecting the anticrossings.

2. Then we set the rest point frequency of the qubit based on the calculated mapping.

3. Finally, we measure the qubit T_1 and phonon T_1 of both mode0 and mode1.

This fitting of the data can not be performed using only the typical fitting function that consists of an exponential to obtain the T_1 time, because some of the traces contain low-frequency noise and additionally, whenever the qubit is close to a phonon mode there will be oscillations between the qubit and the phonon, similar to the 1D phonon Rabi measurement. To fit the data more precisely we use a fitting function consisting of an exponential times a cosine (the same fitting function is used for the 1D phonon Rabi measurement) and additionally smoothen the data using the Savitzky-Golay filter provided by the Scipy package [33]. The smoothening of the data is shown in Fig. 4.11. In Figures,4.12a, 4.12b and 4.13 we show the result of the fitted T_1 of the qubit, phonon mode0 and phonon mode1 respectively as we change the rest point offset of the qubit. The frequency in the cosine term is fitted to be the lowest frequency component, which is at about 2MHz, and thereby helps to get a more accurate result of the decay time. Note that the red dots indicate when the fit with an exponential times a cosine fails, in which case we choose to fit the data using a simple exponential function. An explanation for why the fit fails is that not in every trace, there is a clear oscillation, making the cosine dependence a hindrance to fitting the data.

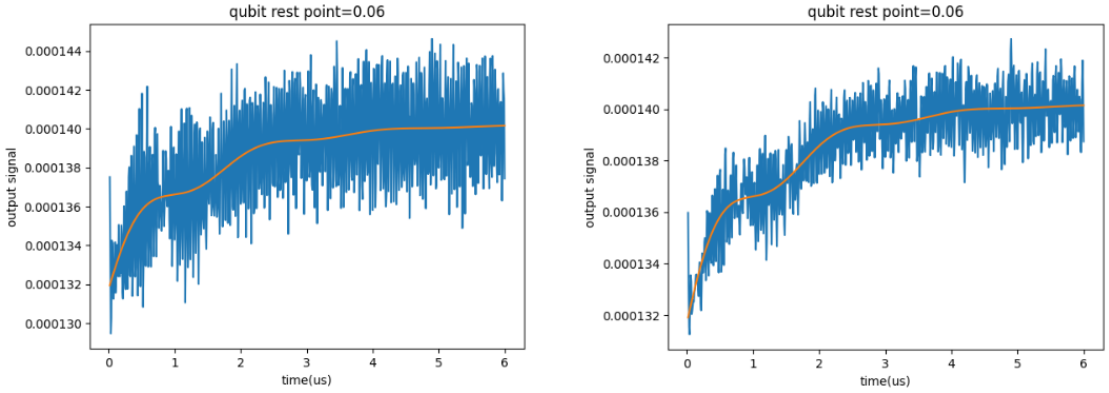

a b

Figure 4.11.: **a:** Phonon T_1 measurement of mode 0. **b:** Same measurement as shown in Figure **a** with the difference that the data has been smoothed using the Savitzky-Golay filter.

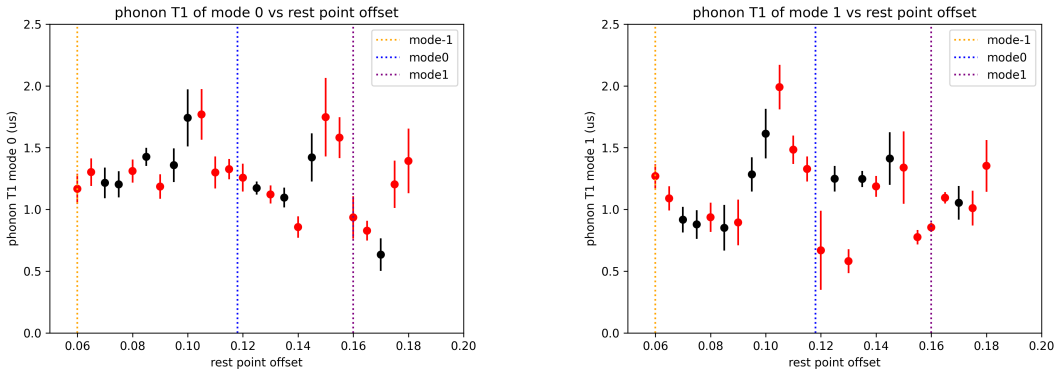

a b

Figure 4.12.: **a:** Phonon T_1 measurement of mode 0 vs rest point offset of the qubit. **b:** Phonon T_1 measurement of mode 1 vs rest point offset of the qubit. For both plots, the data is fitted using an exponential function times a cosine (black data points) to determine the T_1 of the respective T_1 measurement. In case the fit fails, we fit the data using a simple exponential function to extract the T_1 (red data points). The error bars shown here are calculated from the fit of the smoothened data, note that the true uncertainty is higher. The vertical lines indicate the rest point offset applied to the qubit for which the qubit will be resonant with a phonon mode.

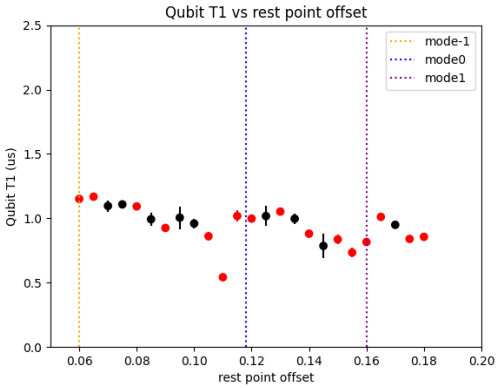

Figure 4.13.: Qubit T_1 vs rest point offset of the qubit. The data is fitted using an exponential function times a cosine (black data points) to determine the T_1 of the respective T_1 measurement. In case the fit fails, we fit the data using a simple exponential function to extract the T_1 (red data points). The error bars shown here are calculated from the fit of the smoothened data, note that the true uncertainty is higher. The vertical lines indicate the rest point offset applied to the qubit for which the qubit will be resonant with a phonon mode.

The interpretation of the data is somewhat difficult due to the very low T_1 times of the device. For example, in 4.13 we see that the qubit T_1 decreases as the qubit is stark shifted closer to mode0 (when we use a rest point offset of 0.118). This is unexpected since when the two modes are close, they effectively hybridize and the T_1 is expected to be an average of the T_1 of the qubit and the phonon. Since the qubit T_1 is slightly smaller than the T_1 of the phonon mode0 as shown in Fig. 4.13, we expected to have a higher qubit T_1 as we move the qubit closer to the phonon mode0.

The analysis presented in this subsection should be repeated once we have a device with increased lifetimes to better understand the behavior of the T_1 times of the qubit and the phonons.

In most of the traces of T_1 measurements, we observed faster as well as slower oscillations, as shown in the trace of Fig. 4.11a. To analyze this, we can perform a Fourier transform of the measured data. In Fig. 4.14 we show the Fourier transform of all T_1 measurements of mode0 obtained via the method described above.

From the plot, we can see a lower frequency component with a frequency of about 2 MHz as well as two frequency components at around 12.5 and 25 MHz. The 12.5 and 25 MHz frequency components can be identified as the phonon FSR of the HBAR, which is typically between 12 and 13 MHz, and its higher harmonic. The coupling strength of 1.38 ± 0.02 MHz is smaller than the FSR, but still not insignificant. Therefore, even when the qubit is far detuned from the phonon mode, the qubit still exchanges energy with the phonon modes. This can be seen in the tail of the chevron pattern in the phonon 2D Rabi measurement shown in Fig. 4.9a. Therefore, for a given qubit frequency the energy can be swapped into multiple phonon modes. Another explanation for the 12.5 and 25 MHz frequency components is that the coupling is coherent, which means the components of the phonon modes will pick up a phase difference proportional to the detuning between the modes. When swapping the excitation back to the qubit mode, this phase difference leads to constructive or destructive interference, which shows in the resulting qubit population. This interference will take place at the frequency differences between the participating phonon modes, which are at multiples of the FSR. The 2 MHz component could be due to added noise from any of the measurement devices or a different experimental artifact. The Fourier transforms of the T_1 measurements of the qubit and phonon mode1 are shown in Figures 4.15 and 4.16. Both of these plots show a similar behavior as previously described.

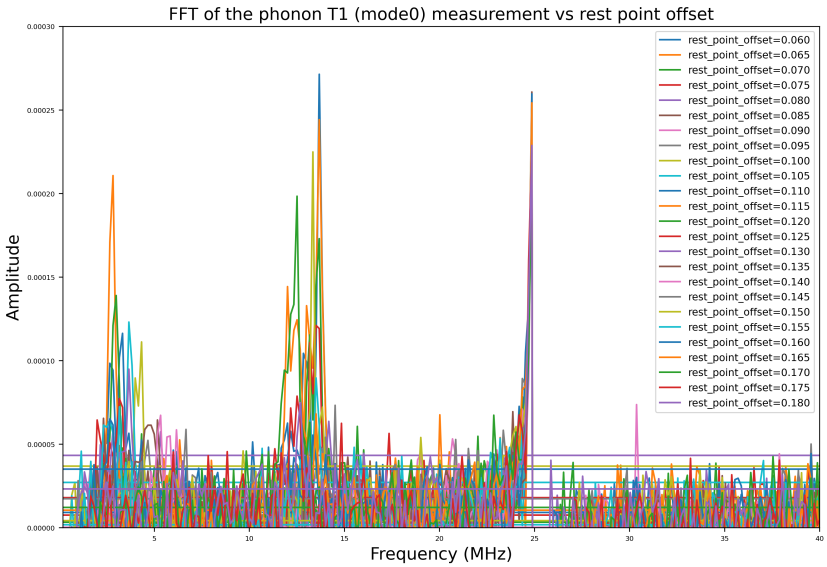

Figure 4.14.: Fourier transform of the T_1 phonon measurements of mode0.

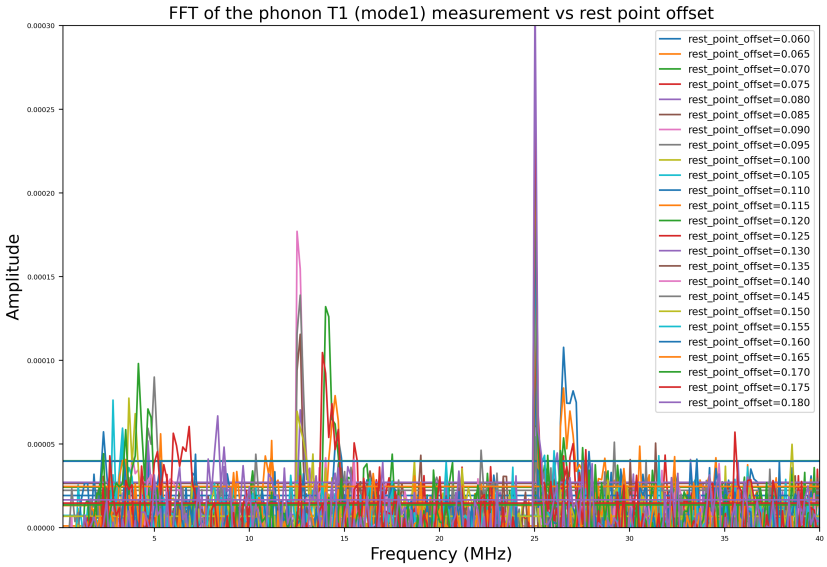

Figure 4.15.: Fourier transform of the T_1 phonon measurements of mode1.

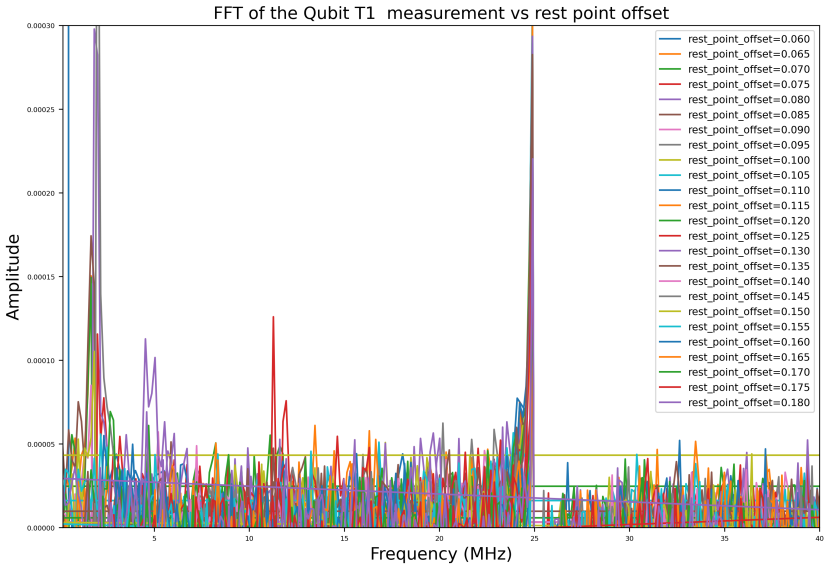

Figure 4.16.: Fourier transform of the T_1 qubit measurements.

4.3.5. Experimental difficulties

The characterization of this device was a time-consuming process that included cooling the sample in two different cooldowns. The measurements during the first cooldown were very noisy and after analyzing the data, we suspected that a cable in the measurement apparatus was broken. Many room temperature cables and eventually all cables inside the dilution refrigerator were measured, until the damaged cable was found. After the damaged cable was replaced and the sample was cooled down again, the noise that we observed during the first cooldown disappeared, confirming that the problem was a damaged cable. The measurements presented throughout this section were all performed during the second cooldown.

Due to the necessity of having short pulse lengths, we had to increase the pin length of the output pin to increase the output coupling ratio, as explained previously. The very low T_1 time requires us to use very short pulses, which require significantly more averaging in all measurements.

Due to the short lifetimes of the qubit, the pulse lengths used in many experiments had to be chosen to be very short. This has the effect that the bandwidth of the pulses are large, thereby possibly exciting neighboring modes. In most experiments, we used a pulse length of 0.2 μs which corresponds to a bandwidth of 5 MHz, thereby while driving the qubit, it is possible that we also drive a neighboring phonon.

Furthermore, in this sample, the antenna of the qubit was not designed to couple only to a single transverse phonon mode. The coupling to many higher-order transverse modes makes the measurements more difficult because the higher-order transverse modes can dephase from each other since they have different frequencies. In other cQAD experiments, the qubit antenna is designed to selectively couple only to the fundamental Laguerre Gaussian mode of the HBAR.

Lastly, after finishing the measurements of this $\hbar$BAR device and performing a reflectometry measurement of the device, we found that there is still a layer of AlN on the entire surface of the HBAR. This can happen due to miscalibration in the fabrication process, specifically in the etching process, where the etching is not performed for a sufficiently long time to remove all AlN from the surface of the HBAR. This layer of piezoelectric AlN can explain the low lifetimes of the device. Specifically, this layer can cause increased dielectric losses in the piezo or undesired phonon radiation via the piezo. Furthermore, due to this layer of piezoelectric AlN on the substrate, the qubit could couple to mechanical modes of the HBAR that live in the entire bulk of the HBAR and not only to the intended modes of the cylindrically shaped resonator formed below the pancake-shaped AlN film. These additional mechanical modes make the interpretation of the results more difficult.

Chapter 5

Conclusion

Throughout this master's thesis, we simulated and measured high-frequency qubits as part of the development of a quantum transducer using an HBAR. We studied and measured the electromechanical coupling of the high-frequency qubit to an HBAR. In chapter 2 the necessary theoretical background to understand the devices measured throughout this work was presented.

In chapter 3 the design of the high-frequency transmon qubit, which includes an on-chip readout resonator, was explained. Simulations of the devices were performed using Ansys as well as the Python pyEPR package. The sensitivity of the qubit chip positioning inside of the tunnel cavity was simulated and shown to be insignificant. A redesign of the on-chip readout resonator was proposed and the simulations performed to achieve the targeted properties of the qubit were explained. This is done by iteratively sweeping the device parameters and simulating the device properties for each iteration of the sweep. Additionally, the electromechanical coupling strength between the qubit and an HBAR was simulated and compared to the measurement results. The simulations qualitatively suggest that the coupling strength is an effective coupling strength to a collective mode that consists of multiple higher-order transverse modes.

In chapter 4 we present the experimental results measured in this work. The experimental procedure to characterize the qubits is detailed in this chapter and the measurement results of three high-frequency transmon qubits are compared. The longest T_1 and T_2 measured were $T_1 = 6.5 \pm 0.7$ μs and $T_2 = 1.8 \pm 0.2$ μs, which is short compared to the lifetimes of transmon qubits which were fabricated with similar methods in recent years in the HYQU group [28]. We discussed possible reasons for the short lifetimes. Finally, an $\hbar$BAR device consisting of a high-frequency transmon flip-chip bonded to an HBAR was measured. We demonstrated an electromechanical coupling of the qubit to the phonon modes of the HBAR and measured an electromechanical coupling strength of 1.38 ± 0.02 MHz. Furthermore, we measured how the lifetimes of the qubit and the phonon modes of the HBAR behave as we change the rest point of the qubit.

In future phases of the quantum transduction project, the proposed redesigned readout resonator should be measured and characterized. The short lifetimes of the qubits still need to be investigated. Possible improvements to the qubit design could be made

with the help of an analysis of the energy participation ratios of different regions of the device. Lastly, the high-frequency qubit should be bonded to an HBAR with a quartz substrate as the envisioned quantum transducer requires a quartz substrate to perform the optomechanical coupling at a frequency that is compatible with the frequencies of the qubit that we studied in this work.

Bibliography

1. Kharel, P. *et al.* High-frequency cavity optomechanics using bulk acoustic phonons. en. *Science Advances* **5,** eaav0582. ISSN: 2375-2548. https://www.science.org/doi/10.1126/sciadv.aav0582 (Apr. 2019).
2. Chu, Y. *et al.* Creation and control of multi-phonon Fock states in a bulk acoustic-wave resonator. en. *Nature* **563,** 666–670. ISSN: 1476-4687. https://www.nature.com/articles/s41586-018-0717-7 (Nov. 2018).
3. Kharel, P. *et al.* Multimode strong coupling in cavity optomechanics. arXiv:1812.06202 [physics]. http://arxiv.org/abs/1812.06202 (Feb. 2019).
4. Doeleman, H. M. *et al.* Brillouin optomechanics in the quantum ground state. *Physical Review Research* **5,** 043140. https://link.aps.org/doi/10.1103/PhysRevResearch.5.043140 (Nov. 2023).
5. Georgescu, I., Ashhab, S. & Nori, F. Quantum simulation. en. *Reviews of Modern Physics* **86,** 153–185. ISSN: 0034-6861, 1539-0756. https://link.aps.org/doi/10.1103/RevModPhys.86.153 (Mar. 2014).
6. Daley, A. J. *et al.* Practical quantum advantage in quantum simulation. en. *Nature* **607,** 667–676. ISSN: 0028-0836, 1476-4687. https://www.nature.com/articles/s41586-022-04940-6 (July 2022).
7. Shor, P. W. Polynomial-Time Algorithms for Prime Factorization and Discrete Logarithms on a Quantum Computer. *SIAM Journal on Computing 26.5* (1995).
8. Grover, L. K. A fast quantum mechanical algorithm for database search. arXiv:quant-ph/9605043. http://arxiv.org/abs/quant-ph/9605043 (Nov. 1996).
9. Suppressing quantum errors by scaling a surface code logical qubit. en. **614,** 676–681. ISSN: 0028-0836, 1476-4687. https://www.nature.com/articles/s41586-022-05434-1 (Feb. 2023).
10. Krinner, S. *et al.* Realizing repeated quantum error correction in a distance-three surface code. en. *Nature* **605,** 669–674. ISSN: 1476-4687. https://www.nature.com/articles/s41586-022-04566-8 (May 2022).
11. Sivak, V. V. *et al.* Real-time quantum error correction beyond break-even. en. *Nature* **616,** 50–55. ISSN: 1476-4687. https://www.nature.com/articles/s41586-023-05782-6 (Apr. 2023).
12. Storz, S. *et al.* Loophole-free Bell inequality violation with superconducting circuits. en. *Nature* **617,** 265–270. ISSN: 1476-4687. https://www.nature.com/articles/s41586-023-05885-0 (May 2023).

13. Valivarthi, R. *et al.* Teleportation Systems Toward a Quantum Internet. *PRX Quantum* **1,** 020317. https://link.aps.org/doi/10.1103/PRXQuantum.1.020317 (Dec. 2020).

14. DiVincenzo, D. P. & IBM. The Physical Implementation of Quantum Computation. *Fortschritte der Physik* **48.** arXiv:quant-ph/0002077, 771–783. ISSN: 00158208, 15213978. http://arxiv.org/abs/quant-ph/0002077 (Sept. 2000).

15. Mirhosseini, M., Sipahigil, A., Kalaee, M. & Painter, O. Superconducting qubit to optical photon transduction. en. *Nature* **588,** 599–603. ISSN: 1476-4687. https://www.nature.com/articles/s41586-020-3038-6 (Dec. 2020).

16. Forsch, M. *et al.* Microwave-to-optics conversion using a mechanical oscillator in its quantum ground state. en. *Nature Physics* **16,** 69–74. ISSN: 1745-2481. https://www.nature.com/articles/s41567-019-0673-7 (Jan. 2020).

17. Chu, Y. & Gröblacher, S. A perspective on hybrid quantum opto- and electromechanical systems. *Applied Physics Letters* **117,** 150503. ISSN: 0003-6951. https://doi.org/10.1063/5.0021088 (Oct. 2020).

18. Chu, Y. *et al.* Quantum acoustics with superconducting qubits. en. *Science* **358,** 199–202. ISSN: 0036-8075, 1095-9203. https://www.science.org/doi/10.1126/science.aao1511 (Oct. 2017).

19. Blais, A., Grimsmo, A. L., Girvin, S. & Wallraff, A. Circuit quantum electrodynamics. *Reviews of Modern Physics* **93,** 025005. https://link.aps.org/doi/10.1103/RevModPhys.93.025005 (May 2021).

20. Krantz, P. *et al.* A quantum engineer's guide to superconducting qubits. *Applied Physics Reviews* **6,** 021318. https://doi.org/10.1063/1.5089550 (June 2019).

21. Koch, J. *et al.* Charge-insensitive qubit design derived from the Cooper pair box. en. *Physical Review A* **76,** 042319. ISSN: 1050-2947, 1094-1622. https://link.aps.org/doi/10.1103/PhysRevA.76.042319 (Oct. 2007).

22. Knoll, J. Design and simulation of a superconducting qubit coupled to a bulk acoustic wave resonator. *Semester thesis at the HYQU group.* https://ethz.ch/content/dam/ethz/special-interest/phys/solid-state-physics/hyqu-dam/documents/semester-report-Jonathan-Knoll.pdf (2022).

23. Adinolfi, F. Towards microwave to optical transduction for superconducting qubits. *Master thesis at the HYQU group.* https://ethz.ch/content/dam/ethz/special-interest/phys/solid-state-physics/hyqu-dam/documents/master-thesis-Francesco-Adinolfi.pdf (2021).

24. Blais, A., Huang, R.-S., Wallraff, A., Girvin, S. M. & Schoelkopf, R. J. Cavity quantum electrodynamics for superconducting electrical circuits: An architecture for quantum computation. *Physical Review A* **69,** 062320. https://link.aps.org/doi/10.1103/PhysRevA.69.062320 (June 2004).

25. Nakamura, Y., Pashkin, Y. A. & Tsai, J. S. Coherent control of macroscopic quantum states in a single-Cooper-pair box. *Nature* **398,** 786–788. ISSN: 0028-0836, 1476-4687. http://arxiv.org/abs/cond-mat/9904003 (Apr. 1999).

26. Cottet, A. Implementatoin of a quantum bit in a superconducting circuit. *Ph.D. thesis, Universite Paris VI.* http://www.phys.ens.fr/~cottet/ACottetThesis.pdf (2002).

27. Wallraff, A. *et al.* Strong coupling of a single photon to a superconducting qubit using circuit quantum electrodynamics. en. *Nature* **431,** 162–167. ISSN: 1476-4687. https://www.nature.com/articles/nature02851 (Sept. 2004).

28. Von Lüpke, U. *et al.* Parity measurement in the strong dispersive regime of circuit quantum acoustodynamics. en. *Nature Physics* **18,** 794–799. ISSN: 1745-2481. https://www.nature.com/articles/s41567-022-01591-2 (July 2022).

29. Bild, M. *et al.* Schrödinger cat states of a 16-microgram mechanical oscillator. *Science* **380,** 274–278. https://www.science.org/doi/10.1126/science.adf7553 (Apr. 2023).

30. Minev, Z. K. *et al.* Energy-participation quantization of Josephson circuits. en. *npj Quantum Information* **7,** 1–11. ISSN: 2056-6387. https://www.nature.com/articles/s41534-021-00461-8 (Aug. 2021).

31. Michaud, L. Coupling an acoustic resonator to a superconducting qubit using an improved flip-chip bonding process. en. *Semester thesis at the HYQU group.* https://ethz.ch/content/dam/ethz/special-interest/phys/solid-state-physics/hyqu-dam/documents/semester-report-Laurent-Michaud.pdf.

32. Roell, A. Design and Microfabrication of High-Overtone Bulk Acoustic Resonators. *Master's thesis at the HYQU group.*

33. Virtanen, P. *et al.* SciPy 1.0: Fundamental Algorithms for Scientific Computing in Python. *Nature Methods* **17,** 261–272. https://rdcu.be/b08Wh (2020).

34. Banderier, H., Drimmer, M. & Chu, Y. Unified Simulation Methods for Quantum Acoustic Devices. en. *Physical Review Applied* **20,** 024024. ISSN: 2331-7019. https://link.aps.org/doi/10.1103/PhysRevApplied.20.024024 (Aug. 2023).

35. Martienssen, W. & Warlimont, H. *Springer Handbook of Condensed Matter and Materials Data* ISBN: 978-3-540-44376-6 (Jan. 2005).

36. Muralt, P., Conde, J., Artieda, A., Martin, F. & Cantoni, M. Piezoelectric materials parameters for piezoelectric thin films in GHz applications. en. *International Journal of Microwave and Wireless Technologies* **1,** 19–27. ISSN: 1759-0787, 1759-0795. https://www.cambridge.org/core/product/identifier/S1759078709000038/type/journal_article (Feb. 2009).

37. Naghiloo, M. Introduction to Experimental Quantum Measurement with Superconducting Qubits. arXiv:1904.09291 [quant-ph]. http://arxiv.org/abs/1904.09291 (Apr. 2019).

38. Abadal, A. R. Calibration of an IQ mixer for continuous and pulsed modulation. en. *Semester thesis at the QuDev group.* https://qudev.phys.ethz.ch/static/content/science/Documents/semester/Antonio_RubioAbadal_SemesterThesis_140805.pdf.

39. Ambegaokar, V. & Baratoff, A. Tunneling Between Superconductors. *Physical Review Letters* **10,** 486–489. https://link.aps.org/doi/10.1103/PhysRevLett.10.486 (June 1963).

40. Sunada, Y. *et al.* Photon-noise-tolerant dispersive readout of a superconducting qubit using a nonlinear Purcell filter. *PRX Quantum* **5.** arXiv:2309.04315 [quant-ph], 010307. ISSN: 2691-3399. http://arxiv.org/abs/2309.04315 (Jan. 2024).

41. *Grammerly* https://www.grammarly.com.

42. *GitHub Copilot* -https://github.com/features/copilot.

43. *Chat GPT* https://chat.openai.com.

Acronyms

AI artificial intelligence 61

AlN aluminum nitride . . . . . 2, 9–12, 17, 27 f., 30, 32, 42 f., 53

AWG arbitrary wave generator 33

cQAD circuit quantum acoustodynamics . . . . . iii, 2 f., 16, 53

CQED cavity quantum electrodynamics 6

cQED circuit quantum electrodynamics . . . . . 2 f., 6, 17, 32 f.

DASE dimensionality reduced acoustic Schrödingner equation 28, 61

FPGA field programmable gate arrays 33

FSR free spectral range 30, 43, 45, 50

HBAR high-overtone bulk acoustic resonator iii, 2 f., 9–17, 26–32, 40–44, 50, 53 ff., 61

HYQU Hybrid Quantum Systems group at ETH Zurich . . . . 2 f., 15, 26 ff., 41 f., 54

IQ-mixers in-phase and quadrature mixers . . . . . 33 f.

pyEPR python energy-participation ratio package 15, 19, 23, 38, 54

RWA rotating wave approximation 11, 13

SQUID superconducting quantum interference device 3

Appendix A

Appendix

A.1. Higher-order transverse mechanical modes of the HBAR

The first 10 higher-order transverse mechanical modes of the HBAR simulated using the DASE simulation package are shown in Fig. A.1.

A.2. Use of generative Artificial Intelligence throughout this work

Throughout this work, I used artificial intelligence (AI) and generative AI as I declared in the declaration of originality attached in the end of this thesis. Specifically, I used Grammarly [41], GitHub Copilot [42] and ChatGPT [43]. After consultation with my supervisor, I will not cite every instance where one of these tools was used, however, I will give examples of how these tools were used:

- Grammarly was used for correcting spelling and grammar mistakes in this report.
- GitHub Copilot was used for data analysis purposes, specifically the code completion capabilities of GitHub Copilot. For example, the Python code for the data analysis for the plots shown in Figures 4.13and 4.12 was written with the help of GitHub Copilot.
- To debug errors in Python code, for example when plotting or analyzing data, ChatGPT was used.
- ChatGPT was also used to gain insight into some concepts related to this work. An example of a prompt entered into ChatGPT is: "In the context of circuit QED what is the strong dispersive regime and strong coupling regime?".

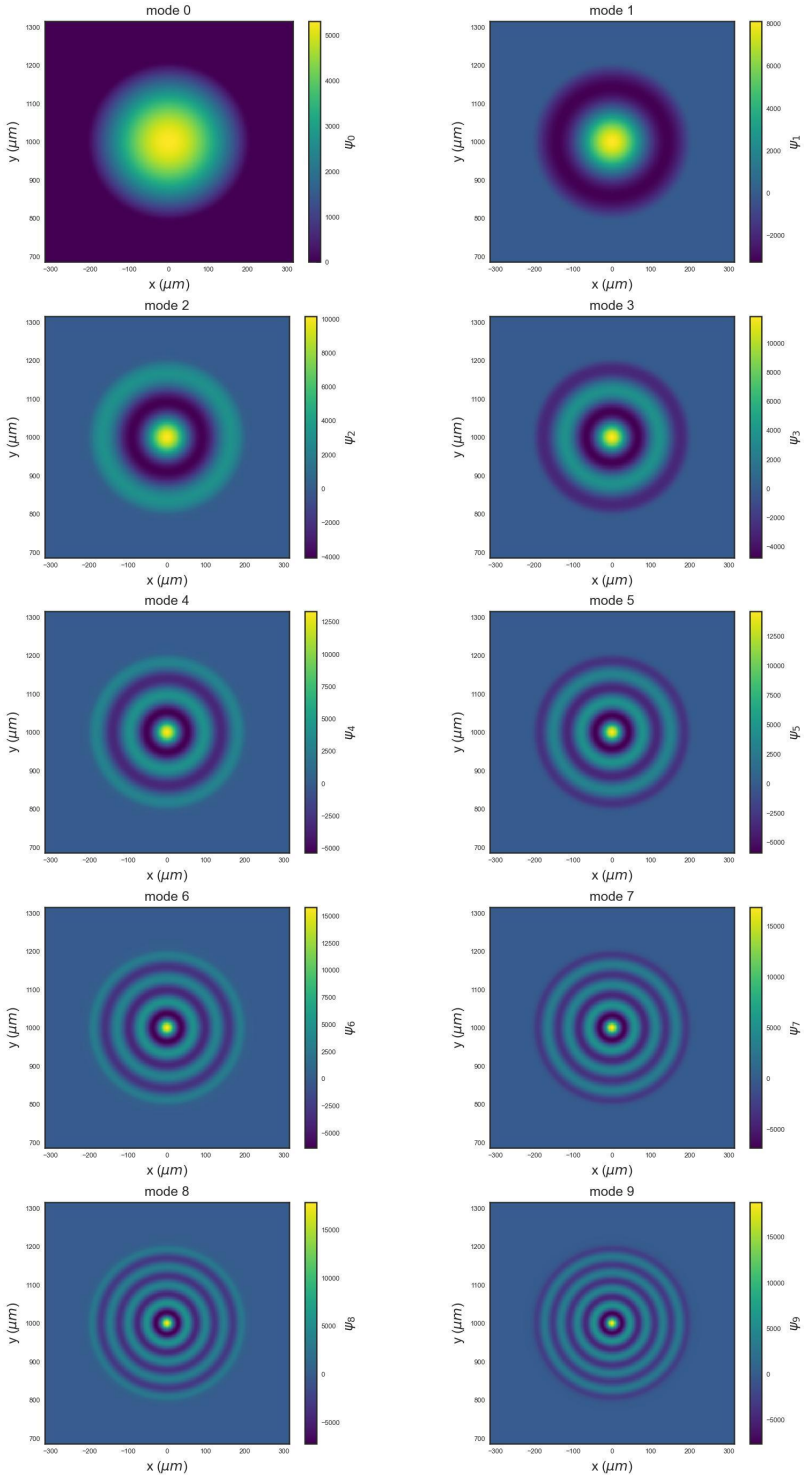

Figure A.1.: Mechanical mode profile for different higher-order transverse modes.